



ESCRT machinery mediates selective microautophagy of endoplasmic reticulum in yeast

Jasmin A Schäfer¹, Julia P Schessner^{1,†}, Peter W Bircham^{1,‡}, Takuma Tsuji², Charlotta Funaya³, Oliver Pajonk¹, Katharina Schaeff¹, Giulia Ruffini¹, Dimitrios Papagiannidis¹, Michael Knop¹ , Toyoshi Fujimoto² & Sebastian Schuck^{1,*} 

Abstract

ER-phagy, the selective autophagy of endoplasmic reticulum (ER), safeguards organelle homeostasis by eliminating misfolded proteins and regulating ER size. ER-phagy can occur by macroautophagic and microautophagic mechanisms. While dedicated machinery for macro-ER-phagy has been discovered, the molecules and mechanisms mediating micro-ER-phagy remain unknown. Here, we first show that micro-ER-phagy in yeast involves the conversion of stacked cisternal ER into multilamellar ER whorls during microautophagic uptake into lysosomes. Second, we identify the conserved Nem1-Spo7 phosphatase complex and the ESCRT machinery as key components for micro-ER-phagy. Third, we demonstrate that macro- and micro-ER-phagy are parallel pathways with distinct molecular requirements. Finally, we provide evidence that the ESCRT machinery directly functions in scission of the lysosomal membrane to complete the microautophagic uptake of ER. These findings establish a framework for a mechanistic understanding of micro-ER-phagy and, thus, a comprehensive appreciation of the role of autophagy in ER homeostasis.

Keywords endoplasmic reticulum; ESCRT machinery; microautophagy; yeast

Subject Categories Autophagy & Cell Death; Membranes & Trafficking

DOI 10.15252/embo.2019102586 | Received 2 June 2019 | Revised 30 October 2019 | Accepted 11 November 2019 | Published online 5 December 2019

The EMBO Journal (2020) 39: e102586

Introduction

Cells profoundly remodel their organelles in response to changing physiological demands. The architecture of the ER in particular undergoes extensive changes during differentiation, stress, and disease. These changes include massive ER expansion when cells boost lipid synthesis or protein secretion (Pathak *et al*, 1986; Wiest *et al*, 1990). ER expansion can be reversed by organelle-selective

autophagy (Bolender & Weibel, 1973; Fumagalli *et al*, 2016). In addition, misfolded proteins in the ER can be eliminated by autophagy (Ishida *et al*, 2009; Forrester *et al*, 2019). Hence, autophagy promotes ER homeostasis by regulating organelle size and mediating protein quality control.

Two types of autophagy appear to be universally conserved in eukaryotes: macro- and microautophagy (Galluzzi *et al*, 2017). During macroautophagy, autophagic cargo is enclosed in autophagosomes, which then fuse with endolysosomes. During microautophagy, autophagic cargo is directly engulfed and taken up by endolysosomes. Both macro- and microautophagy can selectively target certain organelles or operate non-selectively, giving rise to a variety of autophagy pathways.

Macroautophagy requires the core autophagy machinery, a conserved set of proteins essential for autophagosome formation (Mizushima *et al*, 2011; Farré & Subramani, 2016). Organelle-selective macroautophagy additionally involves autophagy receptors, which facilitate inclusion of target organelles into autophagosomes. Many other proteins participate in macroautophagy (Galluzzi *et al*, 2017; Zhao & Zhang, 2019). Of note, endosomal sorting complexes required for transport (ESCRT) proteins are needed for efficient macroautophagy (Filimonenko *et al*, 2007). ESCRTs mediate membrane remodeling and scission in various processes, including multivesicular endosome formation and cytokinesis (Schöneberg *et al*, 2016; McCullough *et al*, 2018). In autophagy, ESCRTs facilitate autophagosome closure, which involves membrane budding away from the cytosol and is therefore topologically equivalent to other ESCRT-mediated processes (Hurley, 2015; Spitzer *et al*, 2015; Takahashi *et al*, 2019; Zhou *et al*, 2019).

Microautophagy is less well understood than macroautophagy. In yeast, the core autophagy machinery is required for microautophagy of peroxisomes and portions of the nucleus (Mukaiyama *et al*, 2002; Krick *et al*, 2008), may be required for microautophagy of lipid droplets under certain conditions (Wang *et al*, 2014; van Zutphen *et al*, 2014; Oku *et al*, 2017), is not required for microautophagy of ER (Schuck *et al*, 2014), and may promote efficiency of

¹ DKFZ-ZMBH Alliance and CellNetworks Cluster of Excellence, Center for Molecular Biology of Heidelberg University (ZMBH), Heidelberg, Germany

² Research Institute for Diseases of Old Age, Juntendo University Graduate School of Medicine, Tokyo, Japan

³ Electron Microscopy Core Facility, Heidelberg University, Heidelberg, Germany

*Corresponding author. Tel: +49 6221 546745; E-mail: s.schuck@zmbh.uni-heidelberg.de

[†]Present address: Department of Proteomics and Signal Transduction, Max Planck Institute of Biochemistry, Martinsried, Germany

[‡]Present address: Laboratory of Systems Biology, VIB Center for Microbiology/Laboratory of Genetics and Genomics, CMPG, KU Leuven, Leuven, Belgium

microautophagy of cytosol (Müller *et al*, 2000; Oku *et al*, 2017). This puzzling picture may be explained, at least in part, by the fact that the term “microautophagy” likely conflates distinct types of autophagy (Schuck *et al*, 2014; Oku & Sakai, 2018). In addition, it remains possible that some microautophagy pathways utilize only part of the core autophagy machinery. Importantly, ESCRT proteins are required for many types of microautophagy (Sahu *et al*, 2011; Liu *et al*, 2015; Oku *et al*, 2017; Tsuji *et al*, 2017; Mejlvang *et al*, 2018). While the topological equivalence of microautophagy and other ESCRT-dependent processes is compelling, a direct involvement of ESCRT machinery in microautophagy has been difficult to demonstrate.

ER-phagy, the selective autophagy of ER, can occur by macroautophagy in both yeast and mammals, and several macro-ER-phagy receptors have been identified (Hamasaki *et al*, 2005; Khaminets *et al*, 2015; Mochida *et al*, 2015; Fumagalli *et al*, 2016; Grumati *et al*, 2017; Smith *et al*, 2018; An *et al*, 2019; Chino *et al*, 2019). Micro-ER-phagy has been found in yeast, in which protein folding stress in the ER induces spherical ER whorls that undergo microautophagy independently of the core autophagy machinery (Schuck *et al*, 2014). At present, the machinery for micro-ER-phagy is unknown, which hinders analysis of its mechanism, clarification of its physiological functions, and assessment of its conservation in mammals.

Here, we define the dynamic membrane rearrangements during micro-ER-phagy in yeast, identify key components of the molecular machinery involved, show that macro- and micro-ER-phagy are genetically separable, parallel pathways and provide evidence that ESCRTs mediate lysosomal membrane scission during microautophagic uptake of ER.

Results

Expression of ER-resident transmembrane proteins can induce micro-ER-phagy

Electron micrographs of yeast treated with the ER stressors DTT or tunicamycin revealed ER whorls as ring-shaped structures (Fig EV1A; Schuck *et al*, 2014). To visualize ER whorls by light microscopy, we imaged yeast expressing the ER marker Sec63-GFP. This approach highlighted pronounced expansion of the organelle during ER stress (Fig EV1B; Schuck *et al*, 2009). However, neither Sec63-GFP nor other transmembrane or luminal ER markers tagged with diverse fluorescent proteins labeled structures resembling whorls. A possible explanation could be that whorls are strongly depleted of certain ER proteins. To address this possibility, we applied freeze-fracture electron microscopy, which visualizes transmembrane proteins as intramembrane particles (Kuby & Wofsy, 1981). Freeze-fracture images revealed DTT-induced multilayered membrane spheres in the cytosol and the vacuole, the yeast lysosome (Fig 1A). Strikingly, these spheres consisted of smooth membranes largely devoid of intramembrane particles, in contrast to regular ER. Hence, ER whorls induced by protein folding stress contain low concentrations of many ER proteins, which complicates their analysis.

ER whorls can also be induced by high-level expression of transmembrane proteins that are genuine ER proteins or are retained in

the ER because of their propensity to oligomerize (Gong *et al*, 1996; Koning *et al*, 1996; Snapp *et al*, 2003; Lingwood *et al*, 2009). We fortuitously found that the vacuolar transmembrane phosphatase Pho8, which dimerizes via its luminal domain (Dancourt & Barlowe, 2009), became such a protein when its cytosolic N-terminus was fused to regular GFP (see Fig EV1C for schematic). At levels exceeding those of endogenous Pho8 by roughly two orders of magnitude, GFP-Pho8 co-localized with Sec63-mCherry, indicating that it was retained in the ER, and induced brightly labeled stretches and rings (Figs 1B and EV1D). No such structures formed in cells that expressed Pho8 fused to strictly monomeric GFP (L221K), which was as abundant as GFP-Pho8 but was still transported to the vacuole membrane (Fig EV1D and E). Many GFP-Pho8 stretches were associated with the vacuole membrane, and about 80% of GFP-Pho8 rings were inside the vacuole. Correlative light and electron microscopy demonstrated that stretches corresponded to stacked cisternal ER and that rings corresponded to whorls (Fig 1C). These whorls consisted of several layers of ribosome-free ER membrane and typically had a diameter of 1.5 μm . Thus, GFP-Pho8 whorls are multilamellar, spherical and targeted by autophagy, similar to whorls formed during ER stress. However, GFP-Pho8 whorls contained various ER proteins (Figs 1B and EV1F). This observation indicates that the mechanisms that restrain protein entry into stress-induced whorls do not apply to GFP-Pho8 whorls. To test whether autophagy of ER whorls induced by GFP-Pho8 reflected a unique phenomenon, we examined the ER transmembrane protein Hmg2-GFP (Fig EV1C). Consistent with earlier studies, high-level expression of Hmg2-GFP yielded ER stretches at the nuclear envelope and the cell cortex as well as ring-shaped ER structures (Fig 1D), which have been shown to represent stacks and whorls, respectively (Wright *et al*, 1988; Koning *et al*, 1996; Fedorovitch *et al*, 2008). Most whorls were in the cytosol, but about 20% were inside the vacuole. We additionally tested whorl formation upon high-level expression of the ER transmembrane proteins Hmg1-GFP, GFP-Cyb5 and P450M4-GFP (Fig EV1C; Wright *et al*, 1988; Vergères *et al*, 1993; Zimmer *et al*, 1997). None of these proteins induced whorls at the expression levels possible in our system (Fig EV1G). Thus, our data suggest that a subset of ER-resident transmembrane proteins can generate ER whorls. In the remainder of this study, we use GFP-Pho8 whorls as an informative substitute for whorls induced by ER stress but validate observations with GFP-Pho8 by analyses under ER stress conditions wherever possible.

To define the membrane dynamics of autophagy of ER whorls, we applied time-lapse imaging. Cells expressing GFP-Pho8 showed ER stacks that were associated with the vacuole membrane, bent toward the vacuole lumen, and were converted into vacuolar whorls (Fig 2A). The time for conversion of bent stacks into vacuolar whorls was 6 min on average but showed a broad, bimodal distribution (Fig EV2A). Whorls inside the vacuole were enclosed by vacuole membrane, showing that they had been taken up by microautophagy. Accordingly, electron micrographs revealed bent ER stacks in large vacuole membrane invaginations (Fig 2B). Occasionally, whorls inside the vacuole appeared as incomplete rings, suggesting that whorls can retain an opening (Fig EV2B). Time-lapse imaging established that the microautophagic process was directional but reversible up to a late stage. Bent stacks in clearly discernible vacuole membrane invaginations, termed uptake

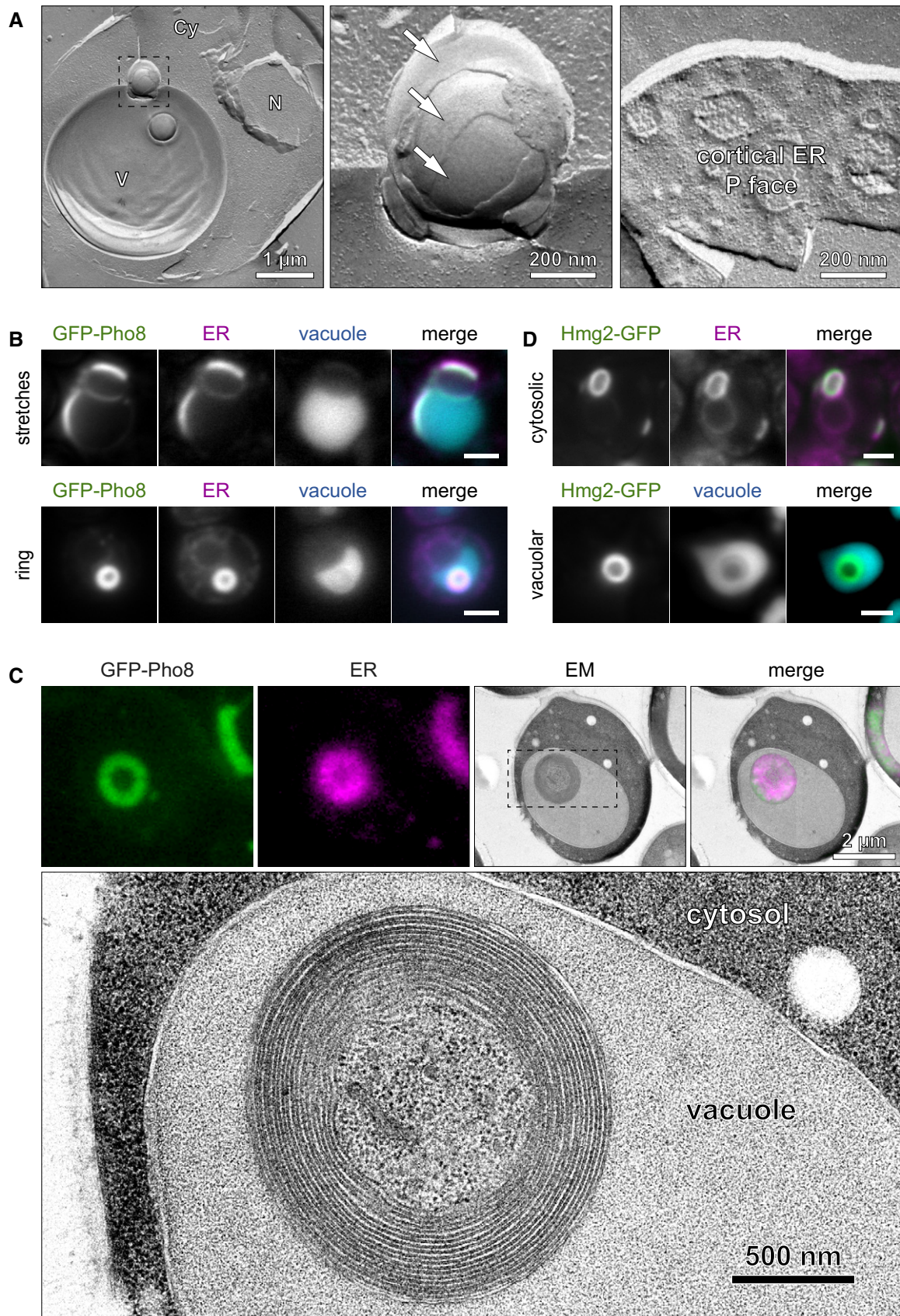


Figure 1.

Figure 1. Expression of ER-resident transmembrane proteins can induce autophagy of ER whorls.

- A Freeze-fracture electron micrograph of wild-type yeast treated with DTT for 3 h. The left panel shows two spherical structures, one in a vacuole membrane invagination and one inside the vacuole. The middle panel shows the boxed area of the left panel at higher magnification. Arrows indicate membrane layers that are free of intramembrane particles. The right panel shows the protoplasmic fracture face (P face) of cortical ER with a high density of intramembrane particles. Cy, cytosol; N, nucleus; V, vacuole.
- B Fluorescence images of cells expressing *GPD* promoter-driven GFP-Pho8 and the ER marker Sec63-mCherry and stained with CMAC to label the vacuole. The upper and lower panels show vacuole-associated and perinuclear GFP-Pho8 stretches and an intravacuolar GFP-Pho8 ring, respectively. Scale bars: 2 μ m.
- C Correlative light and electron microscopy of cells expressing *GPD* promoter-driven GFP-Pho8 and Sec63-mCherry. The lower panel shows the boxed area in the electron micrograph at higher magnification. The ER ring corresponds to a vacuolar whorl and the ER stretch to a perinuclear stack.
- D Fluorescence images of cells expressing Hmg2-GFP and either additionally expressing Sec63-mCherry or stained with CMAC. The upper and lower panels show cytosolic and vacuolar Hmg2-GFP rings, respectively. Scale bars: 2 μ m.

intermediates, had a 90% chance of becoming a vacuolar whorl (Fig 2C). Yet, about 10% of uptake intermediates reverted to vacuole-associated stacks. Even structures that seemed to be vacuolar whorls could revert to uptake intermediates and then to vacuole-associated stacks or cytosolic whorls (Fig 2D). Due to limited temporal and spatial resolution, we were unable to determine whether such whorls had completed the uptake process, including vacuole membrane scission, or had simply remained in long-lived vacuole membrane invaginations. Finally, cytosolic whorls sometimes formed from ER stacks at the cell cortex (Fig EV2C). Autophagy of these whorls was not observed, although we cannot rule out that it occurred with low frequency. Taken together, the use of GFP-Pho8 confirmed that autophagy of ER whorls occurs by microautophagy, revealed that stacks are precursors of whorls, and showed that whorls can form during uptake into the vacuole.

The Nem1-Spo7 complex and ESCRTs are key components for micro-ER-phagy

We previously showed that autophagy of ER whorls during protein folding stress does not depend on the core autophagy machinery (Schuck *et al*, 2014). Likewise, autophagy of GFP-Pho8 whorls did not require the autophagy proteins Atg1, 6, 7, 8, 14, or 16 (Figs 3A and EV3A and B). The macro-ER-phagy receptors Atg39 and 40, which link ER subdomains to the core autophagy machinery (Mochida *et al*, 2015), were also dispensable (Fig EV3C). To identify molecular machinery for micro-ER-phagy, we conducted a genetic screen. We introduced GFP-Pho8 and Sec63-mCherry into the yeast knockout collection, visually screened for mutants with aberrant whorl formation and obtained 119 hits. Among the hits were over twenty genes important for vacuole function, including members of the retromer, CORVET, HOPS, Mon1-Ccz1, and Fab1 complexes, the ESCRT machinery, the V-ATPase, and several other proteins involved in vacuolar protein sorting (Table EV1). Defective autophagy of GFP-Pho8 whorls in these mutants could reflect direct roles of the missing genes in micro-ER-phagy or result from indirect effects of disrupted vacuole function. We focused on the ER-resident protein phosphatase Nem1, the vacuolar phosphatidylinositol-3-phosphate 5-kinase Fab1 and ESCRTs because their removal yielded strong phenotypes and earlier reports had indicated their involvement in autophagy (Rusten *et al*, 2007; Sahu *et al*, 2011; Wang *et al*, 2014). Mutants lacking these proteins still generated ER stacks, but generation of vacuolar whorls was strongly reduced or abolished (Figs 3B and EV3D and E). Cells lacking Nem1 still formed vacuolar whorls, but these were morphologically aberrant

and frequently contained vacuole lumen, occurred in multiples in the same vacuole, or both (Fig EV3D–F).

To test whether these mutants were also defective in ER-phagy during protein folding stress, we employed a previously established biochemical assay. This assay is based on the phosphatase domain of Pho8, called Pho8 Δ 60, fused to the ER membrane protein Yop1 as part of the ER-phagy reporter Yop1-Pho8 Δ 60 (Schuck *et al*, 2014). In contrast to endogenous Pho8, in which the phosphatase domain is luminal, fusion to Yop1 tethers Pho8 Δ 60 to the cytosolic surface of the ER (Fig EV4A). Cytosolic Pho8 Δ 60 has low catalytic activity due to an autoinhibitory C-terminal propeptide. This propeptide is cleaved off only upon autophagic transport into the vacuole, yielding an active enzyme. Interestingly, Yop1-Pho8 Δ 60 showed the expected localization to the peripheral ER but was non-functional (Fig EV4B and C). Nevertheless, since Yop1 is redundant with Rtn1 (Voeltz *et al*, 2006) and its tagging with Pho8 Δ 60 caused no noticeable growth or ER morphology phenotypes, Yop1-Pho8 Δ 60 is a suitable reporter for micro-ER-phagy. Cells were treated with tunicamycin to induce ER-phagy, and Yop1-Pho8 Δ 60 activity was measured. On a technical note, DTT disrupts vacuolar proteolysis, blocks activation of Yop1-Pho8 Δ 60 and therefore cannot be employed in this assay (Schuck *et al*, 2014). Δ *pep4* mutants, in which vacuolar proteolysis is disrupted genetically, were used to determine background phosphatase activity. Δ *atg7* mutants, in which the core autophagy machinery and hence macroautophagy is disabled, retained 60% of wild-type activity, consistent with our earlier data (Fig 3C; Schuck *et al*, 2014). Candidate genes were tested in a Δ *atg7* background to exclude contributions from macro-ER-phagy. Additional removal of Nem1, its binding partner Spo7, or its substrate Pah1 strongly reduced ER-phagy. The same was true for Fab1 and its activator Vac7, whereas elimination of the Fab1 regulators Vac14, Atg18, or Fig 4 had little effect. Removal of ESCRT-0, -I, -II, -III proteins, Bro1, or Vps4 reduced or blocked ER-phagy. Removal of Chm7, an ESCRT protein important for nuclear envelope quality control (Webster *et al*, 2016), had no effect. Hence, genes needed for microautophagy of GFP-Pho8 whorls are also required for micro-ER-phagy induced by protein folding stress.

To address the possibility that the observed ER-phagy defects result from general vacuole dysfunction and impaired removal of the autoinhibitory propeptide from Yop1-Pho8 Δ 60, we measured the activity of endogenous Pho8. Endogenous Pho8 is activated by the same proteolytic processing as Yop1-Pho8 Δ 60 and therefore is an ideal control. Δ *fab1* mutants showed strongly reduced Pho8 activity at steady state and after tunicamycin treatment (Fig 3D and

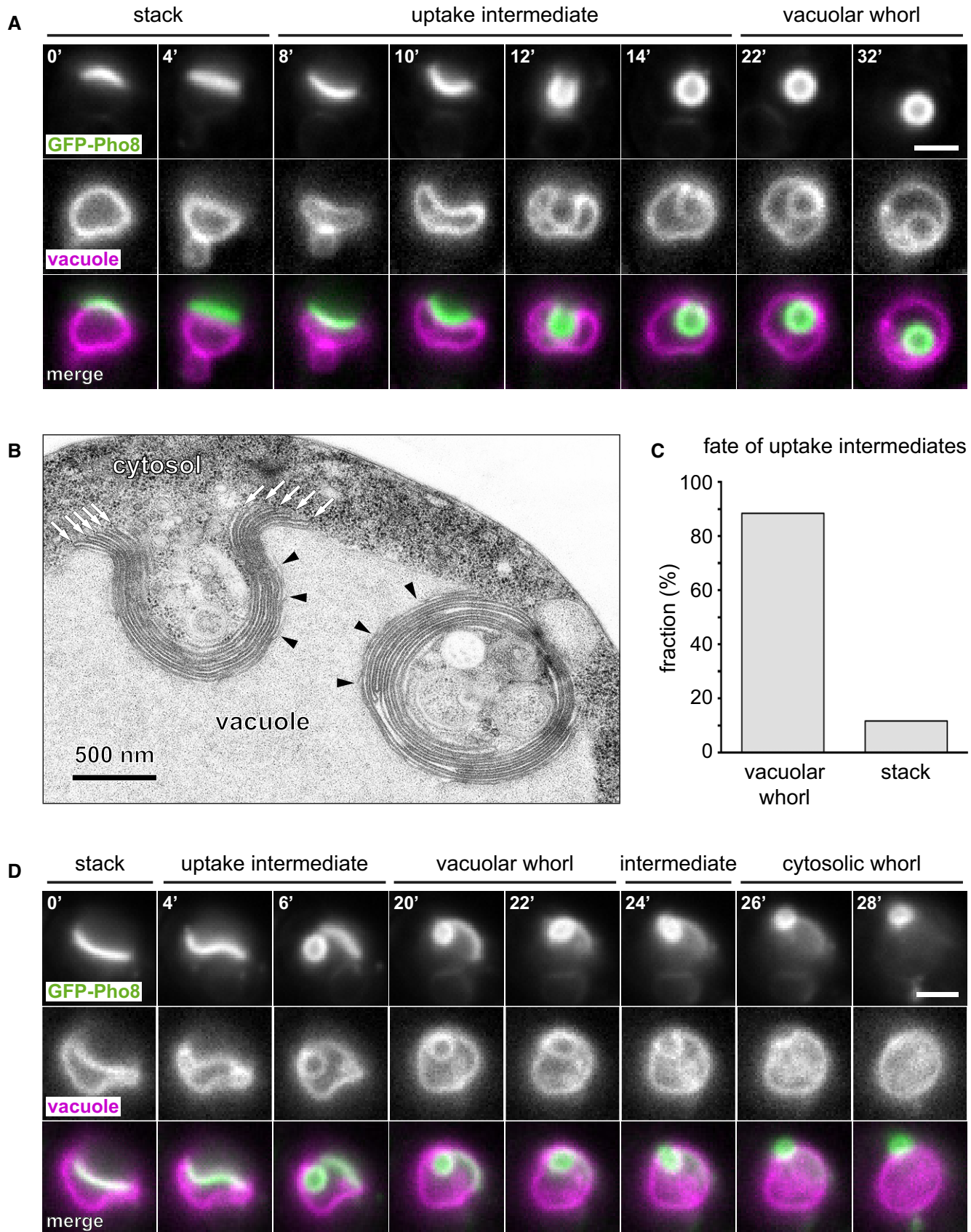


Figure 2.

Figure 2. ER whorls arise from ER stacks and undergo microautophagy.

- A Individual frames from time-lapse imaging of a cell expressing *GAL* promoter-driven GFP-Pho8 and stained with the vacuole membrane dye FM4-64. Numbers indicate the time in minutes after the start of the image sequence. Scale bar: 2 μ m.
- B Electron micrograph of a cell expressing *GPD* promoter-driven GFP-Pho8. Arrows indicate the edges of ER cisternae that are part of a bent stack in a vacuole membrane invagination. Black arrowheads point to vacuole membrane that encases the bent stack and the whorl.
- C Fraction of uptake intermediates that were converted into vacuolar whorls or stacks. $n = 43$.
- D As in panel (A). The image sequence shows formation of a vacuolar whorl that becomes a cytosolic whorl. Scale bar: 2 μ m.

E), suggesting that indirect effects contribute to their ER-phagy phenotype. In contrast, endogenous Pho8 activities in $\Delta nem1$ and ESCRT mutants were reduced by, on average, 30% at steady state and 20% after tunicamycin treatment. Therefore, vacuole functions relevant for Yop1-Pho8 $\Delta 60$ activation are largely intact in $\Delta nem1$ and ESCRT mutants, and it appears unlikely that the mild general defects represented by reduced endogenous Pho8 activities are sufficient to explain the strong inhibition of micro-ER-phagy.

As an alternative assay for ER-phagy, we analyzed cleavage of Sec63-GFP. As reported (Schuck *et al*, 2014), tunicamycin treatment resulted in Pep4-dependent generation of several GFP-containing cleavage products. These included two fragments of about 55 kDa, which did not depend on Atg7 and were used as readout for micro-ER-phagy (Fig 3F). Removal of *Nem1*, *Spo7*, *Snf7*, or *Vps4* in a $\Delta atg7$ background diminished generation of these fragments (Fig 3F and G).

In summary, these biochemical data confirm that the *Nem1-Spo7* complex and ESCRTs are genuine components of the micro-ER-phagy machinery.

Macro- and micro-ER-phagy have distinct molecular requirements

Endoplasmic reticulum stress induces microautophagy of ER whorls in wild-type cells and also in mutants lacking core autophagy components (Schuck *et al*, 2014). In addition to whorls, electron micrographs of DTT-treated wild-type cells also showed that ER transported into the vacuole by macroautophagy appeared as short organelle fragments (Fig 4A). Similar ER fragments in macroautophagic bodies have previously been reported during starvation-induced autophagy (Hamasaki *et al*, 2005). Hence, the morphology of ER that is subject to different types of autophagy differs profoundly. To complement these ultrastructural analyses, we aimed to delineate the contributions of the core autophagy machinery, the *Nem1-Spo7* complex and ESCRTs to different autophagy pathways, namely to non-selective macroautophagy, macro-ER-phagy, and micro-ER-phagy.

First, we measured non-selective autophagy upon nitrogen starvation using the soluble cytosolic reporter cyto-Pho8 $\Delta 60$ (Fig EV4A; Noda *et al*, 1995). Under these conditions, autophagy of cytosol occurs, primarily or exclusively, by macroautophagy (Baba *et al*, 1994). Cyto-Pho8 $\Delta 60$ activity was abolished by deletion of *ATG7*, consistent with a strict requirement for the core autophagy machinery (Fig 4B; Mizushima *et al*, 1998). Deletion of *NEM1* or *SPO7* caused only minor defects, but deletion of the ESCRT components *VPS23*, *SNF7*, or *VPS4* reduced non-selective macroautophagy by > 50%. These defects in ESCRT mutants could be due to a role of ESCRTs in autophagosome closure. Alternatively or additionally, they could reflect that ESCRTs maintain vacuole function during

starvation (Müller *et al*, 2015). Accordingly, endogenous Pho8 activity during nitrogen starvation was reduced by half in ESCRT mutants (Fig EV4D).

Second, we measured ER-phagy upon nitrogen starvation using Yop1-Pho8 $\Delta 60$. Deletion of *ATG7* reduced starvation-induced ER-phagy by 75% (Fig 4C). Since macroautophagy is absent in $\Delta atg7$ cells (Mizushima *et al*, 1998), a different mechanism must account for at least 25% of ER turnover under these conditions. Single deletion of *NEM1* or *SPO7* mildly reduced starvation-induced ER-phagy, and deletion of *ATG7* together with either *NEM1* or *SPO7* caused an almost complete block. Hence, disruption of the core autophagy machinery and the *Nem1-Spo7* complex additively inhibited starvation-induced ER-phagy. This result suggests that the two modules act in separate pathways, which likely correspond to macro- and micro-ER-phagy. Single deletion of ESCRT components reduced starvation-induced ER-phagy by > 60%, and combined disruption of the core autophagy machinery and ESCRT components abolished it. As shown above, Atg7-independent micro-ER-phagy is blocked in ESCRT mutants but contributes only 25% of ER turnover during nitrogen starvation. Therefore, the magnitude of the defects in ESCRT single mutants shows that ESCRT proteins are also needed for efficient macro-ER-phagy.

Third, we used Yop1-Pho8 $\Delta 60$ to analyze ER-phagy induced by ER stress. As seen before, deletion of *ATG7* reduced ER-phagy upon tunicamycin treatment by 40% (Figs 3C and 4D). Thus, Atg7-independent micro-ER-phagy accounts for 60% of ER turnover under these conditions. Single deletion of *NEM1* or *SPO7* eliminated roughly 60% of ER-phagy activity and combined deletion of *ATG7* and either *NEM1* or *SPO7* reduced ER-phagy by about 90%. A parsimonious explanation for these results is that the core autophagy machinery and the *Nem1-Spo7* complex function largely in parallel also during ER stress. Single deletion of ESCRT components strongly reduced ER-phagy, which can again only be explained by impairment of both Atg7-independent micro-ER-phagy and Atg7-dependent macro-ER-phagy.

Last, we tested Atg39 and Atg40, which mediate macroautophagy of perinuclear and peripheral ER, respectively (Mochida *et al*, 2015). Deletion of *ATG40* reduced Yop1-Pho8 $\Delta 60$ activity (Figs 4E and EV4E), consistent with localization of Yop1 to the peripheral ER (Voeltz *et al*, 2006). However, *ATG40* deletion had no effect in $\Delta atg7$ cells. Hence, Atg40 is dispensable for Atg7-independent micro-ER-phagy.

Collectively, these results indicate that macro- and micro-ER-phagy are parallel pathways. Their relative contributions to ER turnover depend on how ER-phagy is triggered and their molecular requirements are overlapping yet distinct. The core autophagy machinery is essential for macro-ER-phagy but dispensable for micro-ER-phagy. The *Nem1-Spo7* complex is primarily involved in micro-ER-phagy, although it makes a minor contribution to macro-

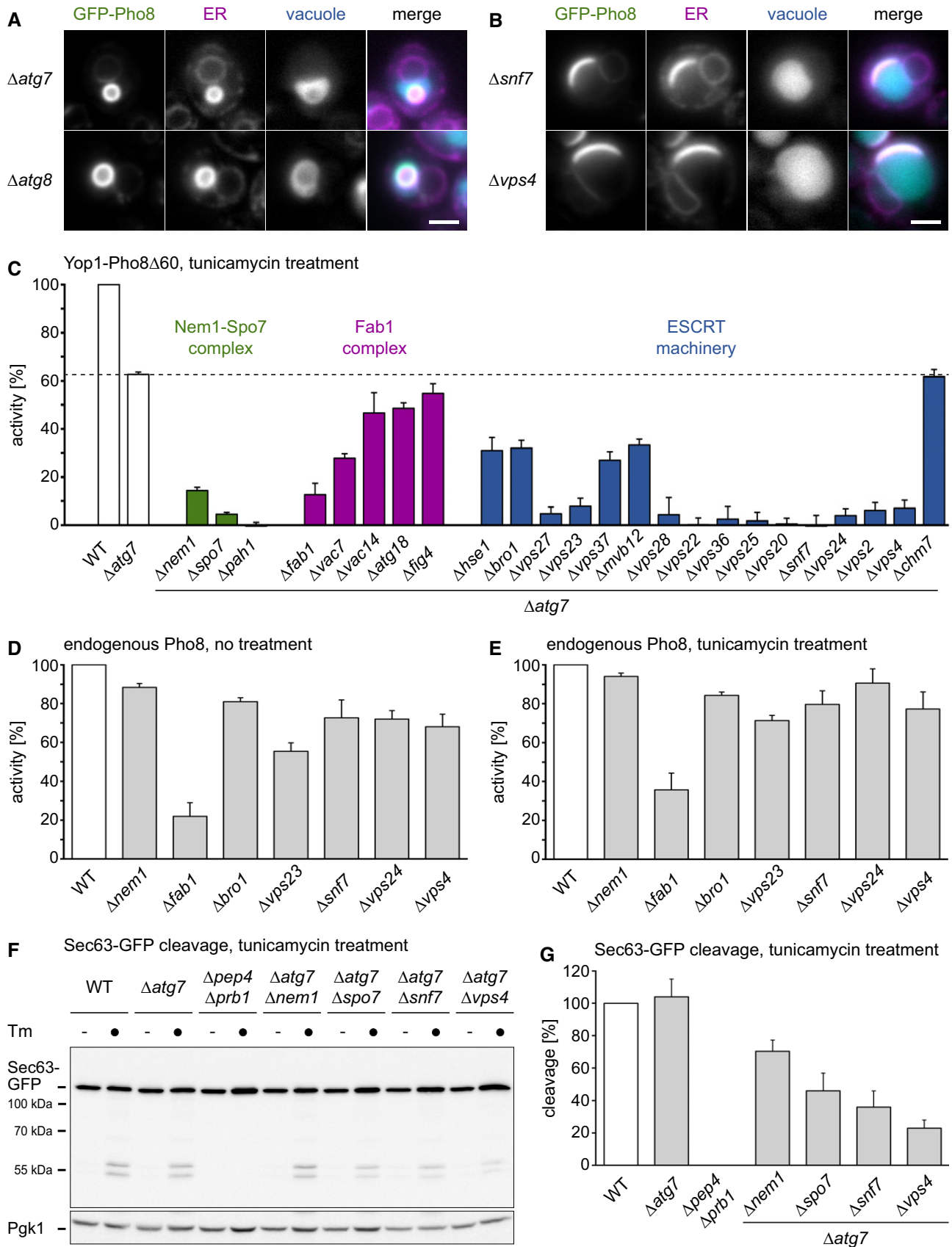


Figure 3.

Figure 3. The Nem1-Spo7 complex and ESCRTs are key components for micro-ER-phagy.

- A, B Fluorescence images of $\Delta atg7$ and $\Delta atg8$ cells (A) or $\Delta snf7$ and $\Delta vps4$ cells (B) expressing GAL promoter-driven GFP-Pho8 and the ER marker Sec63-mCherry and stained with CMAC to label the vacuole. Scale bar: 2 μ m.
- C Relative activity of the ER-phagy reporter Yop1-Pho8 Δ 60 in tunicamycin-treated cells. The dotted line indicates the activity in $\Delta atg7$ cells. Mean + SEM, $n \geq 3$.
- D, E Relative activity of endogenous Pho8 in untreated cells (D) or after tunicamycin treatment (E). Background activity determined in $\Delta pho8$ mutants was subtracted from the activity in all other strains. Mean + SEM, $n = 3$. WT, wild-type.
- F Western blot of GFP from cells expressing Sec63-GFP and treated with tunicamycin (Tm) where indicated. The two Atg7-independent cleavage products of around 55 kDa were used as readout for micro-ER-phagy. Pgk1 served as a loading control.
- G Quantification of Sec63-GFP cleavage normalized to the WT from Western blots as shown in panel (F). Mean + SEM, $n = 4$.

Source data are available online for this figure.

ER-phagy as well. ESCRTs are essential for micro-ER-phagy and are additionally needed for maximum efficiency of macro-ER-phagy and non-selective macroautophagy.

To begin to address the physiological roles of macro- and micro-ER-phagy, we analyzed the growth of wild-type, $\Delta atg39 \Delta atg40$, $\Delta snf7$, and $\Delta snf7 \Delta atg39 \Delta atg40$ cells. No major differences were observed under normal growth conditions (Fig 4F). Combined deletion of *ATG39/40* did not affect growth in the presence of tunicamycin in a wild-type background but further crippled growth in a $\Delta snf7$ background (Fig 4G). This result indicates that the ESCRT machinery and macro-ER-phagy cooperate to promote resistance to ER stress. Since ESCRTs have a variety of functions, direct investigation of the potential links between macro- and micro-ER-phagy will require the identification of ways to specifically disrupt micro-ER-phagy.

ESCRTs mediate vacuole membrane dynamics during micro-ER-phagy

To understand the role of ESCRTs in micro-ER-phagy, we performed time-lapse imaging of wild-type, $\Delta vps23$, $\Delta snf7$, and $\Delta vps4$ cells. GFP-Pho8 expression levels and the fraction of cells with GFP-Pho8 structures were similar in wild-type cells and ESCRT mutants (Figs EV5A and 5A). GFP-Pho8 structures were classified as stacks (at the vacuole membrane, nuclear envelope, or cell periphery), cytosolic whorls, uptake intermediates (bent stacks in vacuole membrane invaginations), or vacuolar whorls (circular and inside the vacuole). In wild-type cells, 80% of GFP-Pho8 structures were classified as stacks, < 5% as cytosolic whorls, < 5% as uptake intermediates, and 15% as vacuolar whorls (Fig 5B). The fraction of cytosolic whorls was increased rather than decreased in $\Delta vps23$, $\Delta snf7$, and $\Delta vps4$ cells, showing that ESCRTs are not required for whorl formation in the cytosol. In contrast, the fraction of vacuolar whorls was sharply reduced to 2% or less, with $\Delta snf7$ cells showing the most severe phenotype. Rare instances of vacuolar whorl formation in ESCRT mutants showed that the process occurred via the same morphological stages as in wild-type cells (Fig EV5B). Since stacks at the vacuole membrane are precursors for vacuolar whorls, we asked whether the association of ER stacks with the vacuole was affected in ESCRT mutants. The fraction of vacuole-associated stacks was 70% in wild-type cells but only 30% in cells lacking Snf7 (Fig 5C). Vacuole-associated stacks in $\Delta snf7$ cells did not co-localize with the enlarged late endosomes present in these mutants, indicating that microautophagy of ER is spatially distinct from multivesicular endosome formation (Fig EV5C). Overall, these results show that ESCRT proteins are major mediators of the microautophagic uptake of ER into the vacuole.

To define at which steps during vacuolar uptake of ER the ESCRT machinery acts, we imaged Snf7, which is the core component of ESCRT-III assemblies (Schöneberg *et al*, 2016; McCullough *et al*, 2018). Tagged Snf7 is non-functional but can serve as a valid tracer of ESCRT action when present alongside endogenous Snf7 (Adell *et al*, 2017). To minimize the risk of dominant negative effects, we introduced, into wild-type cells, an expression construct for Snf7-mNeonGreen under the *VPS24* promoter, which is about threefold weaker than the *SNF7* promoter (Fig EV5D). We confirmed that Snf7-mNeonGreen was functionally neutral because it neither impaired nor supported multivesicular endosome formation or micro-ER-phagy (Fig EV5E and F). Furthermore, we made GFP-Pho8 compatible with visualization of Snf7-mNeonGreen by mutating its chromophore, yielding non-fluorescent GFP(Y66F)-Pho8. Finally, we employed mCherry-Ubc6 as an ER marker, stained the vacuole with CMAC, triggered micro-ER-phagy by expression of GFP(Y66F)-Pho8, and performed time-lapse imaging. Snf7 puncta abruptly appeared adjacent to late ER uptake intermediates, remained associated for some time, and rapidly disappeared, leaving behind vacuolar whorls free of Snf7 (Fig 5D, white arrows, and Movie EV1). We detected a Snf7 punctum at nearly 80% of vacuolar whorls. The duration of Snf7 appearance was highly variable and occasionally as short as a single 2-min movie frame (Figs 5E and EV5G). Interestingly, the same whorl could be visited by Snf7 multiple times, possibly reflecting non-productive recruitment events (Adell *et al*, 2017). Inspection of optical sections covering entire GFP-Pho8 structures confirmed that Snf7 puncta associated with the periphery of ER whorls and not their interior (Movie EV1). Furthermore, Snf7 puncta juxtaposed to ER whorls were typically oriented toward the neck of vacuole membrane invaginations (Fig 5D, black arrow, Fig 5F, and Movie EV2). This transient association of Snf7 with sites of ER uptake suggests that the ESCRT machinery is directly involved in a late step of uptake but is released before uptake is complete. Snf7 puncta appeared close to ER stacks after they had already been bent into whorls. This observation indicates that Snf7 acts subsequent to vacuole membrane bending and ER whorl formation, and at the time when scission of the vacuole membrane occurs.

The above results suggested a revised interpretation of data we had reported previously. Specifically, we had found vacuolar whorls in electron micrographs of DTT-treated $\Delta vps23$ and $\Delta vps4$ cells and concluded that the ESCRT machinery is not essential for micro-ER-phagy (Schuck *et al*, 2014). Given the role of ESCRTs in membrane scission, we tested the possibility that whorls induced by ER stress in ESCRT mutants are trapped in vacuole membrane invaginations. Consistent with our earlier findings, we observed vacuolar whorls

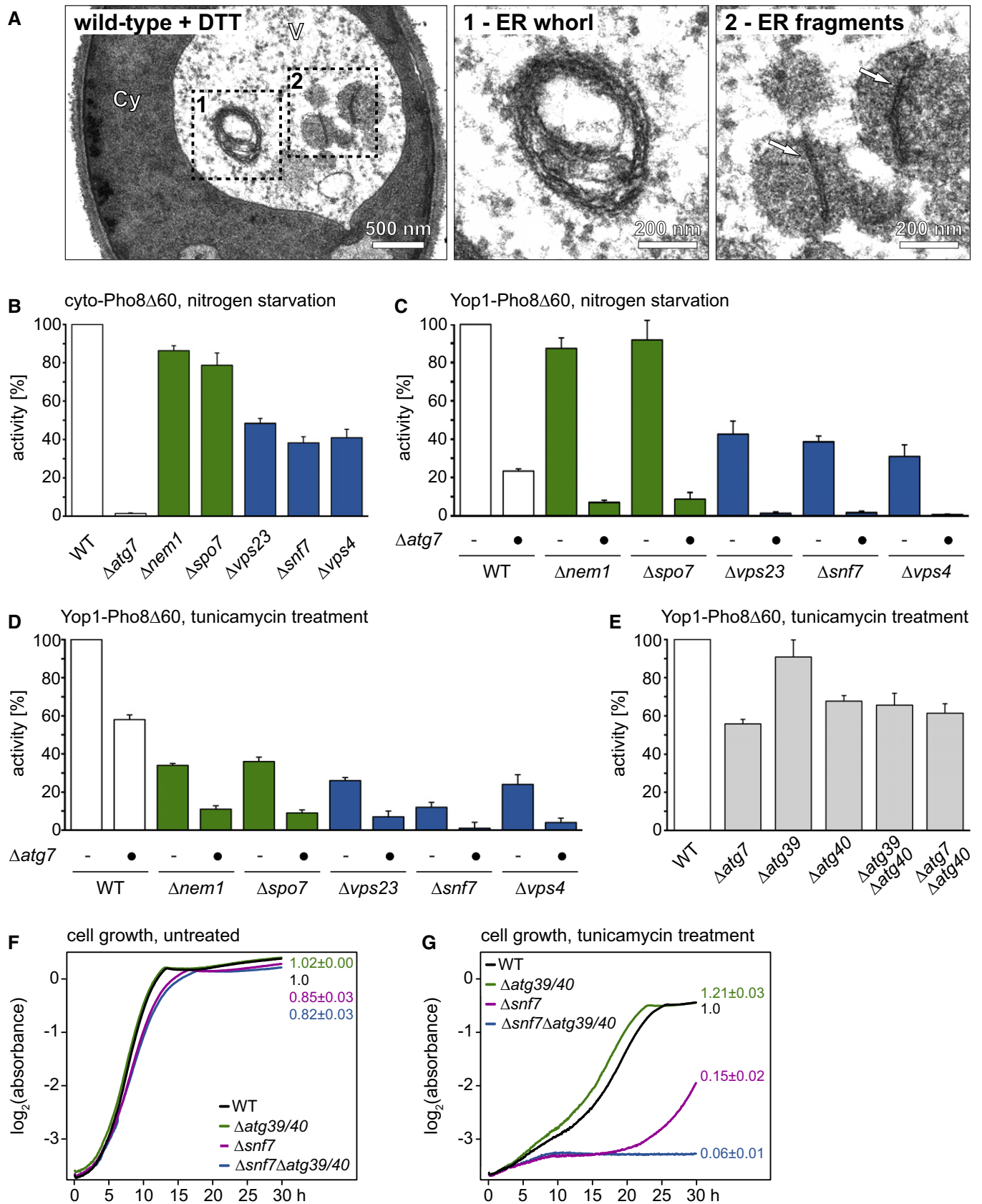


Figure 4.

Figure 4. Macro- and micro-ER-phagy are parallel pathways with distinct morphologies and molecular requirements.

- A Electron micrograph of wild-type yeast treated with DTT for 3 h. Inset 1 shows an ER whorl, and inset 2 shows ER fragments in macroautophagic bodies (white arrows). Cy, cytosol; V, vacuole.
- B Relative activity of cyto-Pho8Δ60 after nitrogen starvation, which reports on non-selective macroautophagy of cytosol. Mean + SEM, $n \geq 3$. WT, wild-type.
- C–E Relative activity of the ER-phagy reporter Yop1-Pho8Δ60 after nitrogen starvation (C) or after tunicamycin treatment (D, E). Mean + SEM, $n \geq 3$.
- F, G Growth assays of untreated and tunicamycin-treated WT, $\Delta atg39/40$, $\Delta snf7$, and $\Delta snf7 \Delta atg39/40$ cells. Numbers indicate growth relative to WT cells based on the areas under the curves. Mean \pm SEM, $n = 3$.

in electron micrographs of DTT-treated $\Delta snf7$ cells, which were indistinguishable from vacuolar whorls in wild-type cells (Fig 6A). However, analysis of serial thin sections revealed that 10 out of 10 vacuolar whorls in $\Delta snf7$ cells were still in contact with the cytosol, showing that uptake of these whorls into the vacuole was incomplete (Fig 6B and C). In contrast, 8 out of 15 vacuolar whorls in wild-type cells were entirely surrounded by vacuole lumen and therefore had completed the uptake process (Fig 6B and D). It is improbable that this difference in the proportions of whorls that had completed uptake arose by chance ($P = 0.008$ according to Fisher's exact test, Fig 6B). Instead, it likely reflects slowed or blocked microautophagic uptake of ER whorls in $\Delta snf7$ cells. These observations indicate that ESCRTs are needed for completion of micro-ER-phagy also during ER stress.

Discussion

We have shown that micro-ER-phagy in yeast involves the conversion of stacked cisternal ER into whorls during uptake into the vacuole. In contrast to macro-ER-phagy, micro-ER-phagy does not need the core autophagy machinery. Instead, the process requires the Nem1-Spo7 complex and ESCRT machinery, which mediates vacuole membrane scission during microautophagic uptake of ER (Fig 7).

In this study, we employed a fusion protein, GFP-Pho8, to trigger microautophagy of ER whorls. Compared with whorls induced by ER stress, GFP-Pho8 whorls have a roughly threefold larger diameter (Schuck *et al*, 2014) and do not recapitulate the intriguing depletion of many ER proteins. Nevertheless, the ER protein content of GFP-Pho8 whorls, their size, slow kinetics of vacuolar uptake and stability inside the vacuole made them a powerful tool for investigating micro-ER-phagy. Importantly, the genes required for microautophagy of GFP-Pho8 whorls are also needed for micro-ER-phagy induced by ER stress. The reduced concentrations of various ER

proteins in stress-induced whorls make biochemical micro-ER-phagy assays difficult. Also, it seems paradoxical that Yop1-Pho8Δ60 is useful because it preferentially localizes to high-curvature tubular ER, whereas whorls consist of low-curvature ER cisternae. However, the presence of an opening in GFP-Pho8 whorls indicates that the edges of the bent ER sheets that make up ER whorls remain unfused. Hence, GFP-Pho8 whorls, and presumably also stress-induced whorls, contain high-curvature sheet edges at their opening. Also, the non-functional Yop1-Pho8Δ60 may be sent for microautophagic degradation because it is misfolded.

ESCRTs mediate membrane remodeling and scission in various processes, for example, during biogenesis of 25-nm intraluminal vesicles at late endosomes in yeast (Henne *et al*, 2013; Adell *et al*, 2017). However, ESCRTs can also participate in the scission of 1- μ m-wide membrane buds, for instance during cytokinesis, and can function at the vacuole membrane in yeast (Henne *et al*, 2013; Zhu *et al*, 2017). Thus, the ESCRT machinery appears to be remarkably flexible, raising the question how it is adapted for micro-ER-phagy and at the same time mediates other processes, including autophagosome closure for macro-ER-phagy. We provide evidence that ESCRT-III is directly involved in vacuole membrane scission. ESCRT-III is recruited to its sites of action by adaptor proteins, for instance by ESCRT-0/I/II for recruitment to late endosomes. The micro-ER-phagy defects observed for various ESCRT mutants closely mirror the relative importance of different ESCRT proteins for multivesicular endosome formation, which is also less strongly affected by loss of Hse1, Bro1, or Mvb12 than by loss of other ESCRT-0/I/II components (Kostelansky *et al*, 2007; Pashkova *et al*, 2013). However, removal of the core ESCRT-I component Vps37 yields only a mild micro-ER-phagy defect, whereas the human Vps37 homolog VPS37A is critical for autophagosome closure (Takahashi *et al*, 2019). These data begin to define the differential use of ESCRTs for multivesicular body formation, macroautophagy, and micro-ER-phagy. Importantly, a large fraction of ESCRT-III components is cytosolic at steady state (Babst *et al*, 2002). This pool may

Figure 5. ESCRT machinery mediates vacuole membrane dynamics during micro-ER-phagy of GFP-Pho8 structures.

- A Fraction of wild-type (WT), $\Delta ups23$, $\Delta snf7$, and $\Delta ups4$ cells with GFP-Pho8 structures. Mean + SEM, $n \geq 3$.
- B Fraction of GFP-Pho8 structures classified as stacks, cytosolic whorls, uptake intermediates, or vacuolar whorls. The number of GFP-Pho8 structures in WT, $\Delta ups23$, $\Delta snf7$, and $\Delta ups4$ cells was 562, 345, 367, and 449, respectively. The table shows the results of chi-square tests for independence for all pairs of strains. ***, highly significant ($P < 0.00001$); ns, not significant ($P > 0.05$).
- C Fraction of stacks classified as peripheral, perinuclear, or vacuole-associated. The number of stacks in WT and $\Delta snf7$ cells was 252 and 351, respectively. The observed distributions in the two strains were analyzed with a chi-square test for independence. ***, highly significant ($P < 0.00001$).
- D–F Fluorescence images of a cell expressing non-fluorescent GFP(Y66F)-Pho8, Snf7-mNeonGreen and the ER marker mCherry-Ubc6, and stained with the vacuole dye CMAC. Numbers indicate the time in minutes after the start of the image sequence. White arrows indicate a Snf7-mNeonGreen punctum adjacent to an ER whorl. Black arrow points to a vacuole membrane invagination. Panel (E) illustrates transient appearance of Snf7 at an ER whorl. Panel (F) illustrates orientation of a Snf7 punctum toward the neck of a vacuole membrane invagination. In this series, mNeonGreen fluorescence was adjusted differently for different time points to compensate for signal decay over time. Scale bar: 2 μ m.

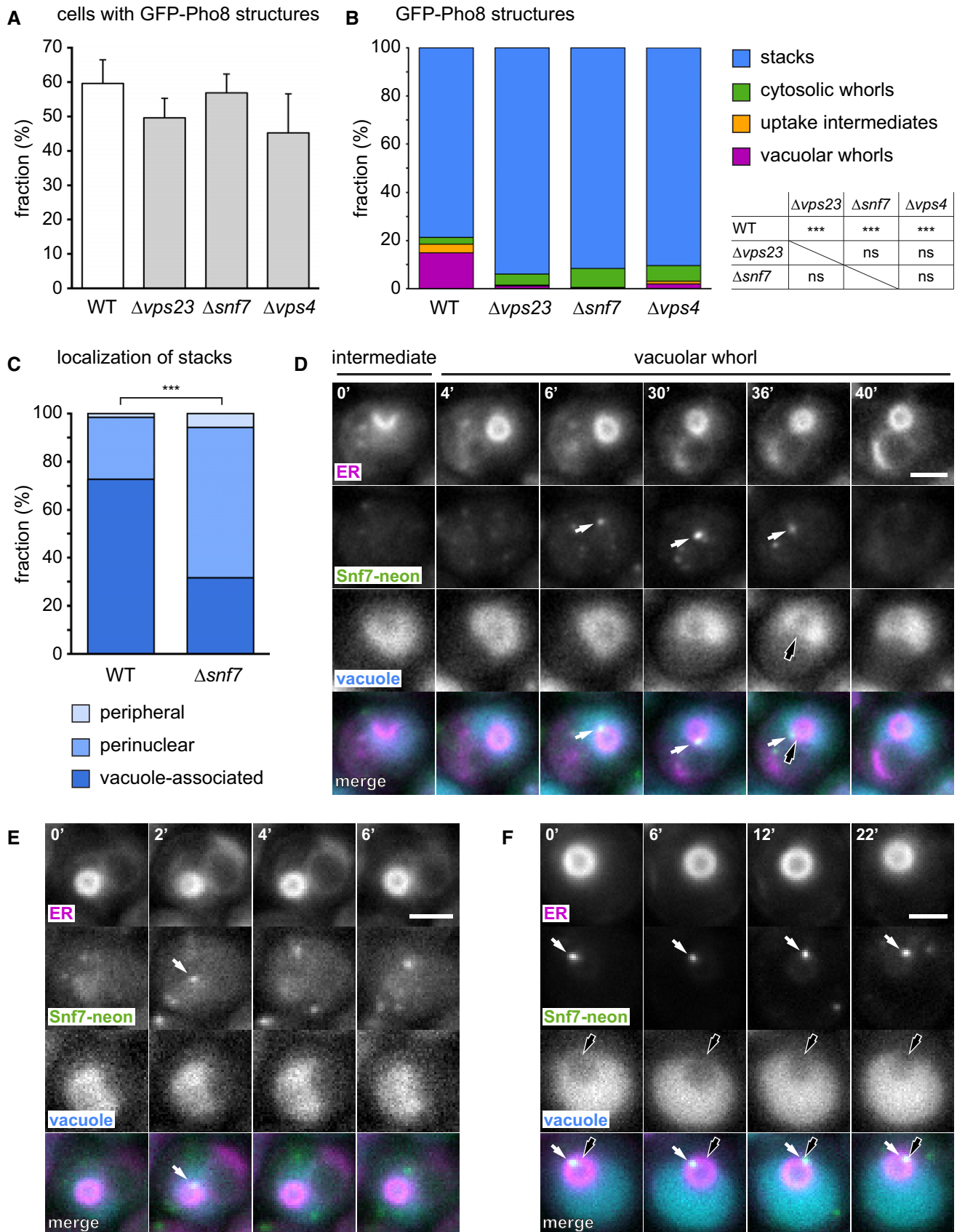


Figure 5.

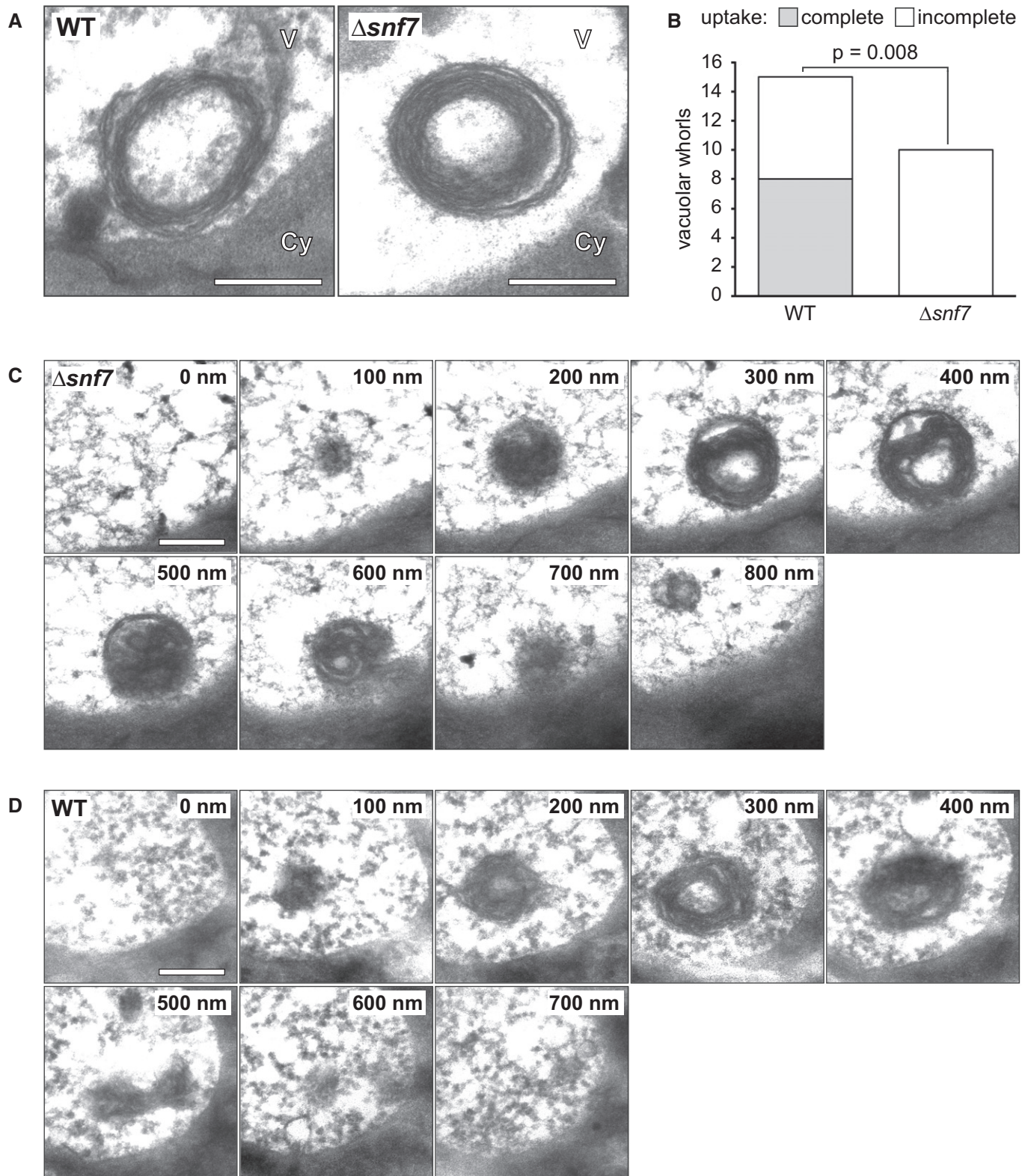


Figure 6. ESCRT machinery is required for completion of microautophagy of ER whorls during ER stress.

- A** Electron micrographs of wild-type and $\Delta snf7$ cells treated with DTT for 3 h. Cy, cytosol; V, vacuole. Scale bars: 300 nm.
- B** Quantification of vacuolar whorls for which the uptake process was complete or incomplete. The observed distributions in the two strains were analyzed with a Fisher's exact test.
- C, D** Electron micrographs of serial thin sections of a $\Delta snf7$ cell (**C**) or a wild-type cell (**D**) treated with DTT for 3 h. Note that the whorl appears separated from the cytosol in some sections (e.g., section 300 nm) but is still in contact with the cytosol (see sections 600 and 700 nm). In the wild-type cell (**D**), the vacuolar whorl is completely separated from the cytosol. Scale bar: 300 nm.

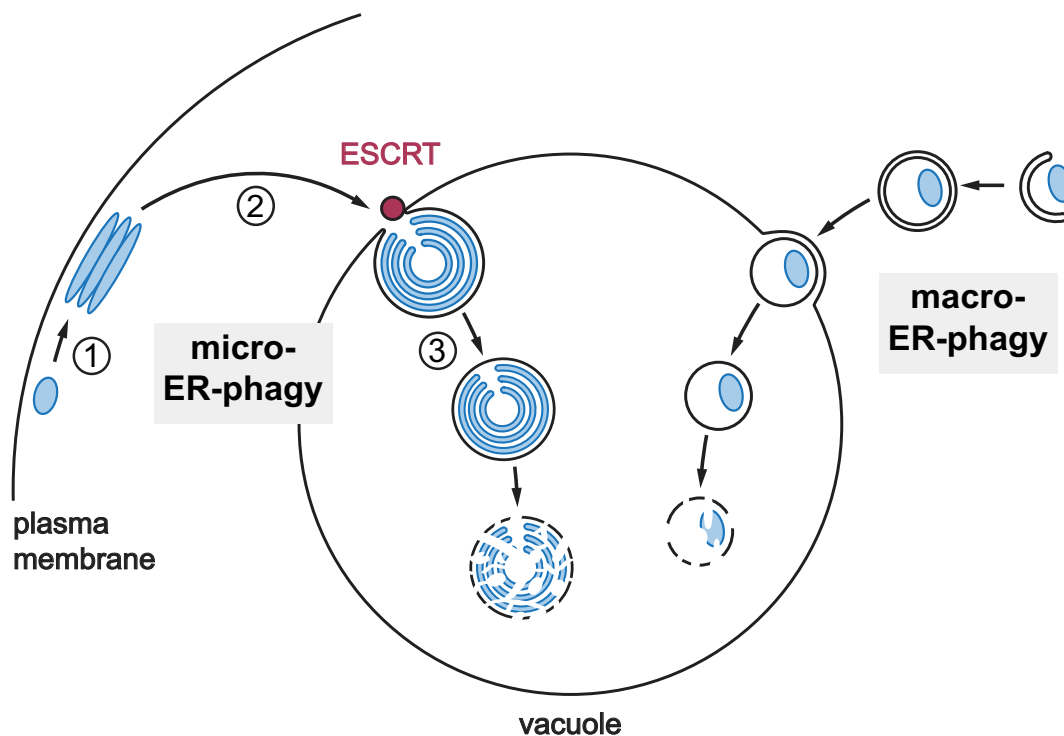


Figure 7. Model of ER-phagy.

During micro-ER-phagy, portions of the ER (blue) are reorganized to form stacks (1). ER stacks are bent, recognized by the vacuole, taken up into vacuole membrane invaginations, converted into whorls, and detached from the remainder of the ER (2). The order of these events is uncertain. ESCRT machinery is recruited to sites of ER whorl uptake and mediates scission of the vacuole membrane (3). In parallel, macro-ER-phagy can also selectively target the ER, which is mediated by the core autophagy machinery.

serve as a reserve that can be used without inhibiting other ESCRT-dependent processes. Although we show that vacuole function is largely intact in ESCRT mutants during ER stress, it is difficult to exclude that disruption of the ESCRT machinery also has indirect effects. Moreover, ESCRTs may have additional direct roles in micro-ER-phagy. The impaired vacuole association of GFP-Pho8 stacks and the reduced formation of uptake intermediates in ESCRT mutants could reflect that ESCRTs also act in these earlier steps. Conceivably, ESCRTs might even mediate the ER membrane scission that is necessary to physically separate stacks from the remainder of the ER (Mast *et al*, 2018). Residual formation of bent stacks and whorls occurs in ESCRT mutants, pointing to additional mechanisms. Intriguingly, the Nem1-Spo7 complex appears to be generally involved in microautophagy and is required for formation of vacuole membrane domains (Toulmay & Prinz, 2013; Tsuji *et al*, 2017; Rahman *et al*, 2018). Such domains are sites of microautophagy of lipid droplets and the line tension at domain boundaries may drive membrane bending (Lipowsky, 2002; Wang *et al*, 2014; Tsuji *et al*, 2017). Whether domain-induced budding is important for micro-ER-phagy remains to be elucidated.

The extensive reorganization of membranes during the formation of ER whorls raises many interesting questions. Exclusion of certain ER proteins from stacks and whorls has been reported before (Gong *et al*, 1996; Koning *et al*, 1996; Okiyoneda *et al*, 2004; Federovitch *et al*, 2008), but our freeze-fracture electron microscopy data are the first to indicate that ER whorls can be almost free of transmembrane

proteins. The underlying mechanisms are unknown but may serve to spare well-folded ER proteins from degradation and could determine the selectivity of micro-ER-phagy regarding protein cargo. Whorl formation has been proposed to involve zippering of ER membranes by proteins that self-interact in trans (Gong *et al*, 1996; Snapp *et al*, 2003). Additional structural features, such as the ability to multimerize, may be important because only a subset of GFP-tagged membrane proteins was capable of inducing ER whorls in our experimental system, consistent with previous analyses (Koning *et al*, 1996; Federovitch *et al*, 2008). Furthermore, it is unclear how membrane zippering might occur for whorls induced by ER stress and which ER determinants enable recognition of stacked ER by the vacuole membrane. Finally, the force that bends stacks into micrometer-sized whorls remains to be identified. As mentioned above, one possibility is that this force is provided, at least in part, by domain-induced budding of the vacuole membrane.

Our study opens up micro-ER-phagy for mechanistic analysis and has general implications for microautophagy and ER homeostasis. Microautophagy has remained enigmatic, in part because it is an umbrella term for distinct pathways. However, our findings support a unifying view that ESCRTs have direct roles in many, perhaps all, microautophagy pathways. By interfering with the metazoan homologues of ESCRTs and the Nem1-Spo7 complex, it is now possible to explore the conservation of micro-ER-phagy (Omari *et al*, 2018) and further investigate the physiological functions of the process. Autophagy eliminates excess ER in both yeast and mammalian cells

(Bolender & Weibel, 1973; Schuck *et al*, 2014; Fumagalli *et al*, 2016). Intriguingly, the selective autophagic elimination of excess ER in mammals has been documented to involve the formation of whorl-like ER structures (Bolender & Weibel, 1973), although the type of autophagy involved remains to be determined. The finding that proteins can be segregated from ER subdomains that give rise to whorls emphasizes the remarkable selectivity of whorl formation and it will be interesting to investigate whether similar mechanisms operate in mammals. In addition, the identification of molecular machinery for micro-ER-phagy will allow to determine whether also mammalian macro- and micro-ER-phagy can occur simultaneously and how they are differentially employed depending on physiological conditions. Finally, the medical importance of ER-phagy in viral infection, neuropathy, and cancer is just beginning to emerge (Gruhati *et al*, 2018), and understanding both macro- and micro-ER-phagy will help uncover how autophagy promotes organellar and hence organismal health.

Materials and Methods

Plasmids

Plasmids used in this study are listed in Appendix Table S1, and sequences of oligonucleotides for plasmid construction are given in Appendix Table S2. To generate pRS406-P_{GPD}-GFP-Pho8, pRS406-P_{GPD}-mCherry-Ubc6 was amplified with primers p406 rev GPD overhang/CYCterm fw Pho8 overhang and ligated, by means of the NEBuilder HiFi DNA assembly master mix (New England Biolabs, Ipswich, Massachusetts), with P_{GPD}-GFP-Pho8 amplified with primers GPD-GFPPho8 fw/GFPPho8 rev from genomic DNA of yeast strain SSY1094. The GFP used therefore was codon-optimized yeast-enhanced GFP (yeGFP, Cormack *et al*, 1997). pRS406-P_{GPD}-mGFP-Pho8 containing monomeric GFP(L221K) was generated from pRS406-P_{GPD}-GFP-Pho8 by site-directed mutagenesis with primers yeGFP L221K fw/rev. To generate pRS406-P_{GAL}-GFP-Pho8, pRS406-P_{GPD}-GFP-Pho8 was amplified with primers p406 GFPPho8 fw/p406 GFPPho8 rev and ligated with the GAL promoter sequence amplified from pRS416-P_{GAL} (Mumberg *et al*, 1994) with primers GAL fw overhang/GAL rev overhang. To generate pRS405-P_{GAL}-GFP-Pho8, pRS406-P_{GAL}-GFP-Pho8 was amplified with primers p406 no URA fw/p406 no URA rev to remove the URA3 gene and ligated with the LEU2 gene amplified from pRS415 (Sikorski & Hieter, 1989) with primers LEU2 prom fw overhang/LEU2 cds rev overhang. To generate pRS404-P_{GPD}-mCherry-Ubc6, the expression cassette for mCherry fused to the C-terminal 18 amino acids of Ubc6 was excised from pRS406-P_{GPD}-mCherry-Ubc6 with AatIII/NaeI and cloned into the AatIII/NaeI site of pRS404 (Sikorski & Hieter, 1989). To generate pRS406-P_{GAL}-Hmg2(K6R)-GFP, Hmg2(K6R)-GFP was first amplified from Yip-P_{GAL}-Hmg2(K6R)-GFP (Federovitch *et al*, 2008) with primers Xba-Hmg2/GFP-Bam and cloned into the XbaI/BamHI site of pRS415-P_{ADH} (Mumberg *et al*, 1995), yielding pRS415-P_{ADH}-Hmg2(K6R)-GFP. The Hmg2(K6R)-GFP-T_{CYC} cassette was then excised from pRS415-P_{ADH}-Hmg2(K6R)-GFP with XbaI and KpnI and cloned into the XbaI/KpnI site of pRS406-P_{GAL}-GFP-Pho8, yielding pRS406-P_{GAL}-Hmg2(K6R)-GFP. To generate pRS406-P_{GAL}-GFP-Cyb5, pRS406-P_{GAL}-GFP-Pho8 was linearized with primers CYCterm fw/linker rev and ligated with a gBlock gene fragment (IDT, Leuven, Belgium)

containing the yeast Cyb5 coding sequence. The plasmid pRS406-P_{GAL}-P450M4-GFP was constructed through several intermediates from the pRS406-P_{GAL} backbone, Yep51-P450M4 (Zimmer *et al*, 1997) and yeGFP. To generate pRS416-P_{SNF7}-Snf7-LAP-mNeonGreen, pRS416-Snf7-LAP-eGFP (Adell *et al*, 2017) was amplified with primers Snf7 term fw neon overhang/LAP rev neon overhang to remove the eGFP coding sequence and ligated with mNeonGreen coding sequence amplified from pFA6a-mNeonGreen-kanMX6 with primers neon fw/rev. To generate pRS416-P_{VPS24}-Snf7-LAP-mNeonGreen, pRS416-P_{SNF7}-Snf7-LAP-mNeonGreen was amplified with primers Snf7 VPS24pr overhang fw/backbone VPS24pr overhang rev and ligated with the VPS24 promoter amplified from genomic DNA of strain SSY122 with primers VPS24pr fw/rev. To generate pRS413-P_{GPD}-mCherry-CPS, the P_{GPD}-mCherry-CPS-T_{CYC} cassette was excised from pRS416-P_{GPD}-mCherry-CPS with NaeI and SacI and cloned into the NaeI/SacI site of pRS413-P_{CYC} (Mumberg *et al*, 1995), replacing the CYC1 promoter. pRS405-P_{GAL}-GFP(Y66F)-Pho8 was generated from pRS405-P_{GAL}-GFP-Pho8 by site-directed mutagenesis with primers GFP(Y66F) fw/rev.

Yeast strain generation

Strains are listed in Appendix Table S3 and were derived from W303 MATa unless indicated otherwise. Gene tagging and deletion was done with PCR products (Longtine *et al*, 1998; Janke *et al*, 2004). After inserting plasmids into the genome, clones with the desired number of integrations were selected by flow cytometry. To generate SSY1653, SEC63 in strain Y7092 (Tong & Boone, 2007) was tagged with mCherry, yielding SSY1646. Next, to enable genomic integration of multiple copies of the P_{GAL1}-GFP-Pho8 expression cassette, the deleted URA3 coding sequence in SSY1646 was restored by integration of the wild-type URA3 gene amplified from pRS406-P_{GAL1}-GFP-Pho8 with primers URA3pr fw overhang/URA3ter rev overhang. The newly introduced wild-type URA3 coding sequence was then replaced with the *ura3-1* allele amplified from SSY122 genomic DNA with primers URA3 cds fw and URA3 cds rev. Counterselection with 5-fluoroorotic acid yielded strain SSY1648. Finally, cells were transformed with XcmI-linearized pRS406-P_{GAL1}-GFP-Pho8 and a clone that had integrated four copies of the plasmid was identified by flow cytometry.

Growth conditions

Strains were cultured at 30°C in YPD or SC medium. YPD consisted of 1% yeast extract (Becton Dickinson, Heidelberg, Germany), 2% peptone (Becton Dickinson), and 2% glucose (Merck, Darmstadt, Germany). SC consisted of 0.7% yeast nitrogen base (Sigma, Taufkirchen, Germany), amino acids, and either 2% glucose, 2% raffinose (Sigma) or 1% raffinose/2% galactose (AppliChem, Darmstadt, Germany). Raffinose and galactose were sterile-filtered rather than autoclaved to avoid hydrolysis or caramelization. SC media containing glucose, raffinose or raffinose/galactose are referred to as SCD, SC-raf, or SC-raf/gal, respectively.

Electron microscopy

For conventional chemical fixation, cells were grown to OD₆₀₀ = 0.5 in YPD medium, and either diluted to OD₆₀₀ = 0.1 and left

untreated, or diluted to $OD_{600} = 0.2$ and treated with 8 mM DTT (Roche, Mannheim, Germany). Cells were grown for another 3 h, and 10 ODs of cells were harvested by centrifugation at 1,000 g at room temperature for 5 min and resuspended in 1 ml fixative containing 1% EM grade glutaraldehyde and 0.2% EM grade formaldehyde from Electron Microscopy Sciences (EMS, Munich, Germany) in 40 mM KH_2PO_4 pH 7.0. Cells were incubated for 3 min, pelleted at 1,500 g for 2 min, resuspended in 1 ml fresh fixative, and incubated on ice for 50 min. At room temperature, cells were washed for 3×5 min with water and resuspended in freshly prepared 2% $KMnO_4$ (EMS). Cells were incubated for 3 min, pelleted at 1,500 g for 2 min, resuspended in 1 ml fresh 2% $KMnO_4$, and incubated for 45 min. Cells were dehydrated by consecutive incubations for 5 min each in 50, 70, 80, 90, 95, and 100% (v/v) ethanol (EMS). After a final wash in water-free ethanol, cells were washed for 3×10 min with propylene oxide (EMS) and embedded in EPON resin (Embed-812, EMS). Cells were infiltrated at room temperature with 25% (v/v) resin in propylene oxide for 1 h, followed by 50% resin for 2 h, 75% resin for 4 h, pure resin at 30°C for 1 h, pure resin at 30°C for 2×12 h, and pure resin with 3% accelerator (BDMA, EMS) at 30°C for 12 h. Resin was cured at 60°C for 2 days, and 70–100 nm thin sections were cut and stained with 2% aqueous uranyl acetate for 5 min followed by Reynolds' lead citrate for 3 min. Images were acquired with a Jeol JEM-1400 80 kV transmission electron microscope (Jeol, Tokyo, Japan) equipped with a TemCam F416 digital camera (TVIPS, Gauting, Germany). Serial sections of 100 nm thickness were used for quantification of whorl uptake into the vacuole. Series of electron micrographs were acquired that contained at least one image of a whorl inside the vacuole and covered the whole whorl. Randomly renamed image series of these vacuolar whorls in wild-type and $\Delta snf7$ cells were independently scored by two individuals who did not know the identity of the cells. Whorls were classified as having completed uptake into the vacuole if they were entirely surrounded by vacuole lumen in all sections and sandwiched by one section above and below that showed vacuole interior without the whorl (see sections 0 and 700 nm in Fig 6D). Whorls were classified as not having completed uptake if they were contacted by the darkly stained cytosol, either sideways or from above or below, even if the vacuole membrane was not visible (see sections 600 and 700 nm in Fig 6C). If no consensus was reached by the two analysts, the series in question was discarded as inconclusive.

For freeze-fracture electron microscopy, cells were grown and treated with DTT as above. EM grids impregnated with cells were sandwiched between a 20- μ m-thick copper foil and a flat aluminum disk (Engineering Office M. Wohlwend, Sennwald, Switzerland) and frozen with an HPM010 high-pressure freezer (Leica Microsystems, Wetzlar, Germany) as described (Tsuji *et al*, 2017). The frozen specimens were transferred to the cold stage of a Balzers BAF 400 apparatus and fractured at -105°C under a vacuum of approximately 1×10^{-6} mbar. Replicas were made by electron-beam evaporation of platinum-carbon (1–2 nm) at an angle of 45° followed by carbon (10–20 nm) at an angle of 90° . The replicas were treated with household bleach to remove biological materials, picked up on formvar-coated EM grids, and observed with a Jeol JEM-1011 EM (Jeol) operated at 100 kV. Digital images were captured using a CCD camera (Gatan, Pleasanton, California).

For correlative light and electron microscopy, strain SSY1425 was grown to $OD_{600} = 6.6$ in SCD, diluted to $OD_{600} = 0.2$ in fresh medium, and grown for another 1.5 h. Cells were collected by filtration, transferred into 0.2-mm-deep aluminum carriers (Engineering Office M. Wohlwend, Sennwald, Switzerland), and frozen with a HPM010 high-pressure freezer (Bal-Tec, Liechtenstein). Freeze substitution was done with an EM AFS2 automated freeze substitution system (Leica Microsystems, Wetzlar, Germany). Samples were kept in dry acetone containing 0.1% uranyl acetate at -90°C for 24 h. The temperature was increased to -45°C at a rate of $5^\circ\text{C}/\text{h}$ and maintained at -45°C for another 5 h. Samples were washed with dry acetone for 3×10 min and incubated in 10% Lowicryl resin in dry acetone for 2 h and in 25% resin for another 2 h. Samples were transferred to 50% resin, and the temperature was increased to -35°C at a rate of $5^\circ\text{C}/\text{h}$ and maintained at 35°C for another 2 h. Samples were transferred to 75% resin, and the temperature was increased to -25°C at a rate of $5^\circ\text{C}/\text{h}$ and maintained at -25°C for another 2 h. Samples were incubated in 100% resin at -25°C for 3×10 h. UV polymerization was done at -25°C for 24 h, the temperature was increased to 20°C under UV light within 9 h, and polymerization was continued for another 24 h. Sectioning was done on a Leica UC6 ultramicrotome, and sections were collected on carbon-coated 200 mesh copper grids (Electron Microscopy Sciences, Hatfield, PA). Grids with 90-nm-thick sections were placed on a drop of water, sandwiched between two coverslips, and mounted in a ring holder (Kukulski *et al*, 2012). Fluorescence was imaged on the grid with sections facing the objective using an Olympus IX81 inverted widefield microscope equipped with a Hamamatsu ORCA-R2 camera and an Olympus PI Apo 100 \times /1.45 oil objective lens on the same day as the sections had been cut. Subsequently, grids were stained with 3% uranyl acetate and Reynolds' lead citrate and the identical areas, identified by position on the grid in relation to grid center, were imaged on a Tecnai F20 EM (FEI, Eindhoven, The Netherlands) operating at 200 kV using the SerialEM software package (Mastrorarde, 2005) and an FEI Eagle 4K \times 4K CCD camera. Fluorescence and electron microscopy images were correlated based on morphological features using the ICY plug-in ec-CLEM (Paul-Gilloteaux *et al*, 2017).

Light microscopy

Imaging of strains expressing Sec63-GFP was done as described (Schuck *et al*, 2009). Cells were grown to $OD_{600} = 0.2$ in YPD medium, washed once with SCD medium, and resuspended in the same volume of SCD. Cells were left untreated or were treated with 8 mM DTT, grown for 3 h, and imaged live at room temperature with a spinning disk confocal microscope consisting of a TE2000U inverted microscope (Nikon, Tokyo, Japan), a CSU22 spinning disk confocal (Yokogawa, Tokyo, Japan), a Cascade II:512 camera (Photometrics, Tucson, Arizona), and a Plan Apo VC 100 \times /1.4 oil objective lens (Nikon).

For imaging of strains expressing GFP-Pho8 or GFP(L221K)-Pho8 under the control of the *GPD* promoter (Figs 1B and EV1E), cells were grown to $OD_{600} = 1$ in SCD containing 10 μ M CMAC (Thermo Fisher Scientific), mounted on a glass coverslip, and overlaid with an agarose pad containing SCD medium. For imaging of strains expressing GFP-Pho8 under the control of the *GAL1* promoter (all

other Figures showing GFP-Pho8), cells were grown for 10 h in SC-raf medium and diluted into fresh SC-raf to reach early log phase ($OD_{600} = 0.1\text{--}0.5$) approximately 16 h later. For induction of the *GAL1* promoter, cells were diluted into SC-raf/gal such that they reached $OD_{600} = 2\text{--}3$ after another 24 h. Where indicated, 10 μM CMAC or 1 $\mu\text{g/ml}$ FM4-64 (Thermo Fisher Scientific, St. Leon-Rot, Germany) were added for the last 16 h to stain the vacuole lumen or vacuole membrane, respectively. Cells were mounted on a glass coverslip and overlaid with an agarose pad containing SC-raf/gal medium, thus immobilizing the cells and ensuring adequate nutrient supply for at least another 3 h. Cells expressing Hmg2-GFP, Hmg1-GFP, GFP-Cyb5, and P450M4-GFP under the control of the *GAL1* promoter were grown and mounted in identical fashion. Images were acquired on the Olympus IX81 widefield microscope at room temperature as described above.

Flow cytometry

Cells were cultured as above to induce expression of GFP-Pho8. One-hundred microliter aliquots were taken to measure GFP fluorescence after excitation with a 488 nm laser with a FACS Canto flow cytometer (BD Biosciences, Franklin Lakes, New Jersey). GFP fluorescence was corrected for cell autofluorescence using a strain not expressing GFP and normalized to cell size using the forward scatter.

Western blotting

Cell lysis and Western blotting were done as described (Szoradi *et al.*, 2018). Primary antibodies were mouse anti-Pho8 1D3A10 (Abcam, Cambridge, UK), mouse anti-GFP 7.1/13.1 (Roche, Basel, Switzerland), and mouse anti-Pgk1 22C5 (Abcam).

Time-lapse imaging and image analysis

For time-lapse imaging, cells from up to four different strains were mounted on a glass coverslip with agarose pads as described above and imaged with a Nikon Ti-E widefield microscope equipped with a motorized stage, the Nikon perfect focus system, a 60 \times /1.49 oil immersion lens, and a Flash4 Hamamatsu sCMOS camera. Movies were acquired at a frame rate of one per 2 min over a total imaging period of 2 h. For each frame, two fields of view were imaged for each of the four strains and z-stacks were acquired that consisted of five optical planes spaced 1 μm apart.

Image analysis was done with the Fiji distribution of ImageJ (Schindelin *et al.*, 2012) extended by plug-ins and custom code for image classification (available under SchuckLab/Movie-Analyser on GitHub). Fluorescent images were subjected to rolling-ball background subtraction with a radius of 80 pixels (8.66 μm). For cell tracking, the CMAC-stained vacuole served as reference. First, image drift over time was corrected in *x/y* dimensions using the plug-in Correct 3D drift with a custom modification by its developer to suppress *z*-correction. Next, cells were segmented with the Bernsen method for auto local thresholding with radius set to 15 and parameters 1 and 2 set to 0. Images were de-speckled and holes filled in. The resulting binary mask was used as input for the MTrack2 plug-in, which was modified such that cropped single-cell movies were generated rather than cell movement tracks. For

classification, time-aligned montages of 4 \times 5 cells were generated from single-cell movies that covered frame 30 and at least five preceding and 10 following frames. Single-cell movies of all acquired fields of view were randomized during montage generation, enabling blindfolded analysis of different strains. These montages served as input for manual classification by click recording.

To determine the fraction of cells containing a GFP-Pho8 structure (Fig 5A), montages were generated from 100 randomly chosen single-cell movies per strain and experiment. Cells were classified as containing or not containing a GFP-Pho8 structure (stack, cytosolic whorl, uptake intermediate, and vacuolar whorl) and the fraction of cells with a GFP-Pho8 structure was determined.

For targeted analysis of GFP-Pho8 structures, cells with high GFP-Pho8 levels were selected by creating montages from single-cell movies of cells with GFP intensities between 12,000 and 18,000 arbitrary units. For this, maximum GFP intensities were calculated for all generated single-cell movies within a centered, circular area with diameter covering 80% of the image height and width to exclude neighboring cells from the intensity analysis. Maximum GFP intensities were calculated across all *z*-slices and time frames of the movies, followed by random selection of at least 200 cells per strain within the set intensity range.

For analysis of the distribution of GFP-Pho8 structures (Figs EV3B and E, and 5B), the above pre-selected single-cell movies were used to classify cells according to the presence of stacks, cytosolic whorls, uptake intermediates, and vacuolar whorls that were present at the start of the movie or arose during imaging. Multiple assignments per cell were allowed. If transitions between classes of structures occurred during a movie, the structure in question was assigned to the latest observed step in the process, with the order from early to late being stack to uptake intermediate to vacuolar whorl or stack to cytosolic whorl. The fraction of vacuolar whorls (Fig EV3B and E) or the fraction of each GFP-Pho8 structure (Fig 5B) relative to the total number of GFP-Pho8 structures was determined.

For analysis of the localization of stacks (Fig 5C), the above pre-selected single-cell movies were used to classify cells according to stack type (vacuole-associated, perinuclear, or peripheral). Multiple assignments per cell were allowed. The fractions of vacuole-associated, perinuclear, and peripheral stacks relative to the total number of stacks were determined.

For analysis of uptake intermediate fate (Fig 2C), cells annotated as uptake intermediates or vacuolar whorls in the analysis above were used as input. Single-cell movies showing transitions of uptake intermediates to vacuolar whorls or stacks were counted, uptake intermediates showing no transition were ignored. The fractions of intermediate-to-whorl and intermediate-to-stack conversions relative to the total number of events were determined. The time for conversion of bent stacks to vacuolar whorls (Fig EV2A) was determined from cells showing complete stack-to-intermediate-to-whorl transitions.

To visualize Snf7 localization at sites of whorl uptake (Fig 5D–F), movies were acquired at a frame rate of one per 2 min over a total imaging period of 1 h. Images were processed with the image classification code described above to generate montages of cells that covered frame 15 and at least five preceding and five following frames. For targeted analysis of whorls, cells with high mCherry-

Ubc6 levels were selected by creating montages from single-cell movies of cells with mCherry intensities between 3,000 and 8,000 arbitrary units. For this, maximum mCherry intensities were calculated for all generated single-cell movies within a centered, circular area with diameter covering 50% of the image height and width. Cells with whorls and, if the case, associated Snf7 were annotated by click recording. For kinetic analysis of Snf7 association with uptake sites (Fig EV5G), single-cell movies showing whorl-associated Snf7 were revisited and the duration of each recruitment event was determined.

Microscopy-based genetic screen

Using strain SSY1653, mCherry-tagged *SEC63* and four copies of the *P_{GALI}-GFP-PHO8* expression cassette were introduced into the yeast knockout collection (Open Biosystems, provided by Michael Knop, ZMBH) by synthetic genetic array methodology (Tong & Boone, 2007). For high-throughput microscopy, cells were grown to saturation in 150 μ l SC-raf/gal in 96-well plates. New 1 ml cultures in SC-raf/gal in 96-deep-well plates were inoculated with 20 μ l saturated cultures and grown overnight. One-hundred microliter of the overnight cultures was transferred into new 96-well plates. Cells were treated with 0.2 μ g/ml rapamycin (Sigma) to increase the fraction of cells with a single, fused vacuole and vacuoles were stained with 50 μ M CMAC for 5 h. Five microliter of the cultures was diluted in 90 μ l SC-raf/gal containing low fluorescence yeast nitrogen base without amino acids, folic acid, and riboflavin (Formedium, Norfolk, UK) and 0.2 μ g/ml rapamycin in 96-well glass bottom plates (Brooks Life Sciences, Chelmsford, Massachusetts) coated with concanavalin A, type IV (Sigma). After 1 h of incubation, non-attached cells were removed by aspiration of the supernatant and addition of 180 μ l fresh SC-raf/gal containing low fluorescence yeast nitrogen base and rapamycin. The strain collection was imaged using the Nikon Ti-E widefield microscope described above. Z-stacks with five planes of 1 μ m width were acquired at three fields of view per mutant.

To facilitate subsequent image analysis, automated cell segmentation was performed. Images were loaded into MATLAB, and background fluorescence was locally removed by applying a morphological opening to the images and subtracting the result from the original images. Cells were automatically segmented based on the bright field images. The z-stack with the highest contrast was selected for further processing based on the standard deviation of pixel intensities in the entire image. The coordinates of initial cell objects were identified using a circular Hough transformation and searching for objects with a radius range of 15–25 pixels (1.6–2.7 μ m). A bounding box extending 2.7 μ m beyond these objects was then cropped, and each cell was further processed individually. A strong background correction was applied to the crops by subtracting 1.5 times the local background intensity as determined above. Images were sharpened by unsharp masking, and canny edge detection was applied to create a binary image. A best fit ellipse was calculated by applying a modified version of the algorithm “ellipse detection using 1D Hough transform” by Martin Simonovsky (downloaded from MATLAB file exchange February 16, 2016). Vacuoles were further segmented using the CMAC image. A 3 \times 3 median smoothing filter was applied, and CMAC staining was locally defined as pixels brighter than the average

pixel intensity of a surrounding ring of radius equal to 9 pixels (= 1 μ m). If these pixels were brighter than an empirically defined background threshold, they were designated vacuolar. Objects smaller than 10 pixels in area were removed as noise and segmented vacuole objects were smoothed by morphological closing. Basic cell measurements were then based on these segmented objects and included total cell GFP and RFP intensity across all z-stacks, and total vacuole GFP and RFP intensity as segmented per z-stack.

Using custom MATLAB viewer software, montages were generated containing 90 uniformly arrayed cells per field of view based on the identified cell crops. These montages were more conducive to visual inspection than the original images with a random spread of cells. Images were analyzed visually to identify mutants in which the frequency of GFP-Pho8 stretches and rings clearly differed from the wild-type.

Pho8 assay

Cells were grown to mid log phase (OD_{600} = 0.1–0.5) in YPD medium. For measurement of activity in untreated cells, cultures were diluted to OD_{600} = 0.4 in YPD and grown for 2 h. For measurement of activity in tunicamycin-treated cells, cultures were diluted to OD_{600} = 0.4 in YPD, treated with 1 μ g/ml tunicamycin (Merck), and grown for 9 h. For measurement of activity in nitrogen-starved cells, cells were diluted to OD_{600} = 0.4 in YPD, pelleted by centrifugation at 1,500 g for 5 min, resuspended in water, pelleted again, resuspended in the same volume of SCD-N medium (0.7% yeast nitrogen base without ammonium sulfate from Formedium, Norfolk, UK, and 2% glucose), and grown for 6 h. $\Delta pep4$ strains were additionally treated with 1 mM PMSF to block Pho8 $\Delta 60$ reporter activation. Cells were collected by centrifugation, washed with water, resuspended in 200 μ l cold lysis buffer (20 mM PIPES pH 6.8, 1% Triton X-100, 50 mM KCl, 100 mM KOAc pH 7.5, 10 mM MgSO₄, 10 μ M ZnSO₄, 1 mM PMSF, and complete protease inhibitors from Roche), and disrupted by bead beating with a FastPrep 24 (MP Biomedical, Heidelberg, Germany). Lysates were adjusted to 1, 2, or 4 ODs/100 μ l (endogenous Pho8, cyto-Pho8 $\Delta 60$, or Yop1-Pho8 $\Delta 60$, respectively) in lysis buffer and cleared by centrifugation at 11,000 g for 2 min at 4°C. For each reaction, 50 μ l lysate was combined with 200 μ l reaction buffer (250 mM Tris pH 8.5, 1% Triton X-100, 10 mM MgSO₄, 10 μ M ZnSO₄) containing 1.25 mM *p*-nitrophenyl phosphate (pNPP, Sigma) as substrate and incubated at 37°C for 5–20 min. Reactions were stopped by addition of 250 μ l 1 M glycine/KOH pH 11. Absorption was measured at 405 nm. To correct for background absorption arising from buffer components, lysate components or non-specific pNPP hydrolysis, the absorption of a buffer control (containing no pNPP and no cell lysate), a lysate control (containing no pNPP), and a substrate control (containing no cell lysate) were determined and subtracted from the absorption of the experimental samples. Protein concentration of cell lysates was determined with the BCA assay kit (Thermo Fisher Scientific, Schwerte, Germany). One unit of specific phosphatase activity was defined as 1 nmol *p*-nitrophenol produced per min and mg total protein. To account for background phosphatase activity in strains containing Yop1-Pho8 $\Delta 60$ and cyto-Pho8 $\Delta 60$, the activity in $\Delta pep4$ cells was subtracted from the phosphatase activity in all other samples. Similarly, for measurement of endogenous

Pho8, the activity in $\Delta pho8$ cells was subtracted from the phosphatase activity in all other samples. This background subtraction was especially important for Yop1-Pho8 $\Delta 60$ because its activity in tunicamycin-treated and nitrogen-starved wild-type cells was only 3.4- and 8.1-fold above its corresponding activities in $\Delta pep4$ cells (on average 7.1 versus 2.1 U and 17 versus 2.1 U). The activity of cyto-Pho8 $\Delta 60$ in nitrogen-starved wild-type cells was 17-fold above its corresponding activities in $\Delta pep4$ cells (on average 57 versus 3.4 U). Endogenous Pho8 activity in untreated, tunicamycin-treated, and nitrogen-starved wild-type cells was more than 60-fold above the corresponding background activities in $\Delta pho8$ cells (on average 67 versus 0.9 U, 132 versus 2.1 U, and 155 versus 2.5 U). The remaining activity was expressed as % of the activity in wild-type cells.

Sec63-GFP cleavage assay

Cultures in YPD medium were grown overnight to $OD_{600} = 0.5$. Two new cultures were prepared from each of these cultures, one in 10 ml YPD at $OD_{600} = 0.2$, and one in 5 ml YPD at $OD_{600} = 0.3$. The 10 ml cultures were grown for another 2 h, and the 5 ml cultures were treated with 1 $\mu\text{g/ml}$ tunicamycin and grown for another 8 h. Cells were harvested by centrifugation and processed for Western blotting as described above. For quantification of Sec63-GFP cleavage, exposures without saturated pixels were used. The intensity of the two Pep4-dependent, Atg7-independent cleavage products at about 55 kDa was divided by the sum intensity of these two cleavage products and full-length Sec63-GFP and normalized to the wild-type.

Growth assays

Growth assays were done and analyzed as described (Szoradi et al, 2018). Exponentially growing cells were diluted to $OD_{600} = 0.05$ in SCD with or without 0.6 $\mu\text{g/ml}$ tunicamycin and grown at 30°C for another 30 h. Areas under the growth curves were normalized to the wild-type control.

Expanded View for this article is available online.

Acknowledgements

We thank Randy Hampton, Benoit Kornmann, Wolf-Hagen Schunck, and David Teis for plasmids; the ZMBH Imaging Facility, the Flow Cytometry and FACS facility at the ZMBH and the Heidelberg University Electron Microscopy Core Facility for support; Holger Lorenz for help with image processing; Georg Borner, Karin Schumacher, and David Teis for discussion and advice; and Frauke Melchior, Anne Schlaitz, and all Schookees for comments on the manuscript. This work was funded by a PhD fellowship from the Heidelberg Biosciences International Graduate School to JAS and grant EXC 81 from the Deutsche Forschungsgemeinschaft.

Author contributions

Conceptualization: JAS and SS; Software: PWB and JPS; Investigation: CF, TF, DP, OP, GR, JAS, KS, JPS, SS, and TT; Resources: MK; Writing—Original Draft: JAS and SS; Writing—Review and Editing: all authors.

Conflict of interests

The authors declare that they have no conflict of interest.

References

- Adell MA, Migliano SM, Upadhyayula S, Bykov YS, Sprenger S, Pakdel M, Vogel GF, Jih G, Skillern W, Behrouzi R et al (2017) Recruitment dynamics of ESCRT-III and Vps4 to endosomes and implications for reverse membrane budding. *eLife* 6: e31652
- An H, Ordureau A, Paulo JA, Shoemaker CJ, Denic V, Harper JW (2019) TEX264 is an endoplasmic reticulum-resident ATG8-interacting protein critical for ER remodeling during nutrient stress. *Mol Cell* 74: 891–908
- Baba M, Takeshige K, Baba N, Ohsumi Y (1994) Ultrastructural analysis of the autophagic process in yeast: detection of autophagosomes and their characterization. *J Cell Biol* 124: 903–913
- Babst M, Katzmann DJ, Estepa-Sabal EJ, Meerloo T, Emr SD (2002) Escrt-III: an endosome-associated heterooligomeric protein complex required for mvb sorting. *Dev Cell* 3: 271–282
- Bolender RP, Weibel ER (1973) A morphometric study of the removal of phenobarbital-induced membranes from hepatocytes after cessation of threatment. *J Cell Biol* 56: 746–761
- Chino H, Hatta T, Natsume T, Mizushima N (2019) Intrinsically disordered protein TEX264 mediates ER-phagy. *Mol Cell* 74: 909–921
- Cormack BP, Bertram G, Egerton M, Gow NA, Falkow S, Brown AJ (1997) Yeast-enhanced green fluorescent protein (yEGFP): a reporter of gene expression in *Candida albicans*. *Microbiology* 143: 303–311
- Dancourt J, Barlowe C (2009) Erv26p-dependent export of alkaline phosphatase from the ER requires luminal domain recognition. *Traffic* 10: 1006–1018
- Farré JC, Subramani S (2016) Mechanistic insights into selective autophagy pathways: lessons from yeast. *Nat Rev Mol Cell Biol* 17: 537–552
- Federovitch CM, Jones YZ, Tong AH, Boone C, Prinz WA, Hampton RY (2008) Genetic and structural analysis of Hmg2p-induced endoplasmic reticulum remodeling in *Saccharomyces cerevisiae*. *Mol Biol Cell* 19: 4506–4520
- Filimonenko M, Stuffers S, Raiborg C, Yamamoto A, Malerød L, Fisher EMC, Isaacs A, Brech A, Stenmark H, Simonsen A (2007) Functional multivesicular bodies are required for autophagic clearance of protein aggregates associated with neurodegenerative disease. *J Cell Biol* 179: 485–500
- Forrester A, De Leonibus C, Grumati P, Fasana E, Piemontese M, Staiano L, Fregno I, Raimondi A, Marazza A, Bruno G et al (2019) A selective ER-phagy exerts procollagen quality control via a Calnexin-FAM134B complex. *EMBO J* 38: e99847
- Fumagalli F, Noack J, Bergmann TJ, Cebollero E, Pisoni GB, Fasana E, Fregno I, Galli C, Loi M, Soldà T et al (2016) Translocon component Sec62 acts in endoplasmic reticulum turnover during stress recovery. *Nat Cell Biol* 18: 1173–1184
- Galluzzi L, Baehrecke EH, Ballabio A, Boya P, Bravo San Pedro JM, Cecconi F, Choi AM, Chu CT, Codogno P, Colombo MI et al (2017) Molecular definitions of autophagy and related processes. *EMBO J* 36: 1811–1836
- Gong FC, Giddings TH, Meehl JB, Staehelin LA, Galbraith DW (1996) Z-membranes: artificial organelles for overexpressing recombinant integral membrane proteins. *Proc Natl Acad Sci USA* 93: 2219–2223
- Grumati P, Morozzi G, Hölper S, Mari M, Harwardt MI, Yan R, Müller S, Reggiori F, Heilemann M, Dikic I (2017) Full length RTN3 regulates turnover of tubular endoplasmic reticulum via selective autophagy. *eLife* 6: e25555
- Grumati P, Dikic I, Stolz A (2018) ER-phagy at a glance. *J Cell Sci* 131: jcs217364

- Hamasaki M, Noda T, Baba M, Ohsumi Y (2005) Starvation triggers the delivery of the endoplasmic reticulum to the vacuole via autophagy in yeast. *Traffic* 6: 56–65
- Henne WM, Stenmark H, Emr SD (2013) Molecular mechanisms of the membrane sculpting ESCRT pathway. *Cold Spring Harb Perspect Biol* 5: a016766
- Hu J, Shibata Y, Zhu P-P, Voss C, Rismanchi N, Prinz WA, Rapoport TA, Blackstone C (2009) A class of dynamin-like GTPases involved in the generation of the tubular ER network. *Cell* 138: 549–561
- Hurley JH (2015) ESCRTs are everywhere. *EMBO J* 34: 2398–2407
- Ishida Y, Yamamoto A, Kitamura A, Lamandé SR, Yoshimori T, Bateman JF, Kubota H, Nagata K (2009) Autophagic elimination of misfolded procollagen aggregates in the endoplasmic reticulum as a means of cell protection. *Mol Biol Cell* 20: 2744–2754
- Janke C, Magiera MM, Rathfelder N, Taxis C, Reber S, Maekawa H, Moreno-Borchart A, Doenges G, Schwob E, Schiebel E et al (2004) A versatile toolbox for PCR-based tagging of yeast genes: new fluorescent proteins, more markers and promoter substitution cassettes. *Yeast* 21: 947–962
- Khaminets A, Heinrich T, Mari M, Grumati P, Huebner AK, Akutsu M, Liebmann L, Stolz A, Nietzsche S, Koch N et al (2015) Regulation of endoplasmic reticulum turnover by selective autophagy. *Nature* 522: 354–358
- Koning AJ, Roberts CJ, Wright RL (1996) Different subcellular localization of *Saccharomyces cerevisiae* HMG-CoA reductase isozymes at elevated levels corresponds to distinct endoplasmic reticulum membrane proliferations. *Mol Biol Cell* 7: 769–789
- Kostelansky MS, Schluter C, Tam YYC, Lee S, Ghirlando R, Beach B, Conibear E, Hurley JH (2007) Molecular architecture and functional model of the complete yeast ESCRT-I heterotetramer. *Cell* 129: 485–498
- Krick R, Muehe Y, Prick T, Bremer S, Schlotterhose P, Eskelinen EL, Millen J, Goldfarb DS, Thumm M (2008) Piecemeal microautophagy of the nucleus requires the core macroautophagy genes. *Mol Biol Cell* 19: 4492–4505
- Kuby JM, Wofsy L (1981) Intramembrane particles and the organization of lymphocyte membrane proteins. *J Cell Biol* 88: 591–598
- Kukulski W, Schorb M, Welsch S, Picco A, Kaksonen M, Briggs JA (2012) Precise, correlated fluorescence microscopy and electron tomography of lowicryl sections using fluorescent fiducial markers. *Methods Cell Biol* 111: 235–257
- Lingwood D, Schuck S, Ferguson C, Gerl MJ, Simons K (2009) Generation of cubic membranes by controlled homotypic interaction of membrane proteins in the endoplasmic reticulum. *J Biol Chem* 284: 12041–12048
- Lipowsky R (2002) Domains and rafts in membranes - hidden dimensions of selforganization. *J Biol Phys* 28: 195–210
- Liu X-M, Sun L-L, Hu W, Ding Y-H, Dong M-Q, Du L-L (2015) ESCRTs cooperate with a selective autophagy receptor to mediate vacuolar targeting of soluble cargos. *Mol Cell* 59: 1035–1042
- Longtine MS, McKenzie A, Demarini DJ, Shah NG, Wach A, Brachat A, Philippsen P, Pringle JR (1998) Additional modules for versatile and economical PCR-based gene deletion and modification in *Saccharomyces cerevisiae*. *Yeast* 14: 953–961
- Madrid AS, Mancuso J, Cande WZ, Weis K (2006) The role of the integral membrane nucleoporins Ndc1p and Pom152p in nuclear pore complex assembly and function. *J Cell Biol* 173: 361–371
- Mast FD, Herricks T, Strehler KM, Miller LR, Saleem RA, Rachubinski RA, Aitchison JD (2018) ESCRT-III is required for scissioning new peroxisomes from the endoplasmic reticulum. *J Cell Biol* 217: 2087–2102
- Mastrorade DN (2005) Automated electron microscope tomography using robust prediction of specimen movements. *J Struct Biol* 152: 36–51
- McCullough J, Frost A, Sundquist WI (2018) Structures, functions, and dynamics of ESCRT-III/Vps4 membrane remodeling and fission complexes. *Annu Rev Cell Dev Biol* 34: 85–109
- Mejlvang J, Olsvik H, Svenning S, Bruun J-A, Abudu YP, Larsen KB, Brech A, Hansen TE, Brenne H, Hansen T et al (2018) Starvation induces rapid degradation of selective autophagy receptors by endosomal microautophagy. *J Cell Biol* 217: 3640–3655
- Mizushima N, Noda T, Yoshimori T, Tanaka Y, Ishii T, George MD, Klionsky DJ, Ohsumi M, Ohsumi Y (1998) A protein conjugation system essential for autophagy. *Nature* 395: 395–398
- Mizushima N, Yoshimori T, Ohsumi Y (2011) The role of Atg proteins in autophagosome formation. *Annu Rev Cell Dev Biol* 27: 107–132
- Mochida K, Oikawa Y, Kimura Y, Kirisako H, Hirano H, Ohsumi Y, Nakatogawa H (2015) Receptor-mediated selective autophagy degrades the endoplasmic reticulum and the nucleus. *Nature* 522: 359–362
- Mukaiyama H, Oku M, Baba M, Samizo T, Hammond AT, Glick BS, Kato N, Sakai Y (2002) Paz2 and 13 other PAZ gene products regulate vacuolar engulfment of peroxisomes during micropexophagy. *Genes Cells* 7: 75–90
- Müller O, Sattler T, Flötenmeyer M, Schwarz H, Plattner H, Mayer A (2000) Autophagic tubes: vacuolar invaginations involved in lateral membrane sorting and inverse vesicle budding. *J Cell Biol* 151: 519–528
- Müller M, Schmidt O, Angelova M, Faserl K, Weys S, Kremser L, Pfaffenwimmer T, Dalik T, Kraft C, Trajanoski Z et al (2015) The coordinated action of the MVB pathway and autophagy ensures cell survival during starvation. *eLife* 4: e07736
- Mumberg D, Müller R, Funk M (1994) Regulatable promoters of *Saccharomyces cerevisiae*: comparison of transcriptional activity and their use for heterologous expression. *Nucleic Acids Res* 22: 5767–5768
- Mumberg D, Müller R, Funk M (1995) Yeast vectors for the controlled expression of heterologous proteins in different genetic backgrounds. *Gene* 156: 119–122
- Noda T, Matsuura A, Wada Y, Ohsumi Y (1995) Novel system for monitoring autophagy in the yeast *Saccharomyces cerevisiae*. *Biochem Biophys Res Commun* 210: 126–132
- Okiyoneda T, Harada K, Takeya M, Yamahira K, Wada I, Shuto T, Suico MA, Hashimoto Y, Kai H (2004) Delta F508 CFTR pool in the endoplasmic reticulum is increased by calnexin overexpression. *Mol Biol Cell* 15: 563–574
- Oku M, Maeda Y, Kagohashi Y, Kondo T, Yamada M, Fujimoto T, Sakai Y (2017) Evidence for ESCRT- and clathrin-dependent microautophagy. *J Cell Biol* 216: 3263–3274
- Oku M, Sakai Y (2018) Three distinct types of microautophagy based on membrane dynamics and molecular machineries. *BioEssays* 40: e1800008
- Omari S, Makareeva E, Roberts-Pilgrim A, Mirigian L, Jarnik M, Ott C, Lippincott-Schwartz J, Leikin S (2018) Noncanonical autophagy at ER exit sites regulates procollagen turnover. *Proc Natl Acad Sci USA* 115: E10099–E10108
- Pashkova N, Gakhar L, Winistorfer SC, Sunshine AB, Rich M, Dunham MJ, Yu L, Piper RC (2013) The yeast alix homolog Bro1 functions as a ubiquitin receptor for protein sorting into multivesicular endosomes. *Dev Cell* 25: 520–533
- Pathak RK, Luskey KL, Anderson RG (1986) Biogenesis of the crystalloid endoplasmic reticulum in UT-1 cells: evidence that newly formed endoplasmic reticulum emerges from the nuclear envelope. *J Cell Biol* 102: 2158–2168
- Paul-Gilloteaux P, Heiligenstein X, Belle M, Domart M-C, Larijani B, Collinson L, Raposo G, Salamero J (2017) eC-CLEM: flexible multidimensional registration software for correlative microscopies. *Nat Methods* 14: 102–103

- Rahman MA, Terasawa M, Mostofa MG, Ushimaru T (2018) The TORC1-Nem1/Sp07-Pah1/lipin axis regulates microautophagy induction in budding yeast. *Biochem Biophys Res Commun* 504: 505–512
- Rusten TE, Vaccari T, Lindmo K, Rodahl LMW, Nezis IP, Sem-Jacobsen C, Wendler F, Vincent J-P, Brech A, Bilder D et al (2007) ESCRTs and Fab1 regulate distinct steps of autophagy. *Curr Biol* 17: 1817–1825
- Sahu R, Kaushik S, Clement CC, Cannizzo ES, Scharf B, Follenzi A, Potolicchio I, Nieves E, Cuervo AM, Santambrogio L (2011) Microautophagy of cytosolic proteins by late endosomes. *Dev Cell* 20: 131–139
- Schindelin J, Arganda-Carreras I, Frise E, Kaynig V, Longair M, Pietzsch T, Preibisch S, Rueden C, Saalfeld S, Schmid B et al (2012) Fiji: an open-source platform for biological-image analysis. *Nat Methods* 9: 676–682
- Schöneberg J, Lee I-H, Iwasa JH, Hurley JH (2016) Reverse-topology membrane scission by the ESCRT proteins. *Nat Rev Mol Cell Biol* 18: 5–17
- Schuck S, Prinz WA, Thorn KS, Voss C, Walter P (2009) Membrane expansion alleviates endoplasmic reticulum stress independently of the unfolded protein response. *J Cell Biol* 187: 525–536
- Schuck S, Gallagher CM, Walter P (2014) ER-phagy mediates selective degradation of endoplasmic reticulum independently of the core autophagy machinery. *J Cell Sci* 127: 4078–4088
- Sikorski RS, Hieter P (1989) A system of shuttle vectors and yeast host strains designed for efficient manipulation of DNA in *Saccharomyces cerevisiae*. *Genetics* 122: 19–27
- Smith MD, Harley ME, Kemp AJ, Wills J, Lee M, Arends M, von Kriegsheim A, Behrends C, Wilkinson S (2018) CCGP1 is a non-canonical autophagy cargo receptor essential for ER-phagy and pancreatic ER proteostasis. *Dev Cell* 44: 217–232.e11
- Snapp EL, Hegde RS, Francolini M, Lombardo F, Colombo S, Pedrazzini E, Borgese N, Lippincott-Schwartz J (2003) Formation of stacked ER cisternae by low affinity protein interactions. *J Cell Biol* 163: 257–269
- Spitzer C, Li F, Buono R, Roschztardt H, Chung T, Zhang M, Osteryoung KW, Vierstra RD, Otegui MS (2015) The endosomal protein CHARGED MULTIVESICULAR BODY PROTEIN1 regulates the autophagic turnover of plastids in *Arabidopsis*. *Plant Cell* 27: 391–402
- Szoradi T, Schaeff K, Garcia-Rivera EM, Itzhak DN, Schmidt RM, Bircham PW, Leiss K, Diaz-Miyar J, Chen VK, Muzzey D et al (2018) SHRED is a regulatory cascade that reprograms Ubr1 substrate specificity for enhanced protein quality control during stress. *Mol Cell* 70: 1025–1037.e5
- Takahashi Y, Liang X, Hattori T, Tang Z, He H, Chen H, Liu X, Abraham T, Imamura-Kawasawa Y, Buchkovich NJ et al (2019) VPS37A directs ESCRT recruitment for phagophore closure. *J Cell Biol* 218: 3336–3354
- Tong AHY, Boone C (2007) High-throughput strain construction and systematic synthetic lethal screening in *Saccharomyces cerevisiae*. *Methods Microbiol* 36: 369–707
- Toulmay A, Prinz WA (2013) Direct imaging reveals stable, micrometer-scale lipid domains that segregate proteins in live cells. *J Cell Biol* 202: 35–44
- Tsuji T, Fujimoto M, Tatematsu T, Cheng J, Orii M, Takatori S, Fujimoto T (2017) Niemann-Pick type C proteins promote microautophagy by expanding raft-like membrane domains in the yeast vacuole. *eLife* 6: e25960
- Vergères G, Yen TS, Aggeler J, Lausier J, Waskell L (1993) A model system for studying membrane biogenesis. Overexpression of cytochrome b5 in yeast results in marked proliferation of the intracellular membrane. *J Cell Sci* 106: 249–259
- Voeltz GK, Prinz WA, Shibata Y, Rist JM, Rapoport TA (2006) A class of membrane proteins shaping the tubular endoplasmic reticulum. *Cell* 124: 573–586
- Wang CW, Miao YH, Chang YS (2014) A sterol-enriched vacuolar microdomain mediates stationary phase lipophagy in budding yeast. *J Cell Biol* 206: 357–366
- Webster BM, Thaller DJ, Jäger J, Ochmann SE, Borah S, Lusk CP (2016) Chm7 and Heh1 collaborate to link nuclear pore complex quality control with nuclear envelope sealing. *EMBO J* 35: 2447–2467
- Wiest DL, Burkhardt JK, Hester S, Hortsch M, Meyer DI, Argon Y (1990) Membrane biogenesis during B cell differentiation: most endoplasmic reticulum proteins are expressed coordinately. *J Cell Biol* 110: 1501–1511
- Wright R, Basson M, D'Ari L, Rine J (1988) Increased amounts of HMG-CoA reductase induce 'karmellae': a proliferation of stacked membrane pairs surrounding the yeast nucleus. *J Cell Biol* 107: 101–114
- Zhao YG, Zhang H (2019) Autophagosome maturation: an epic journey from the ER to lysosomes. *J Cell Biol* 218: 757–770
- Zhou F, Wu Z, Zhao M, Murtazina R, Cai J, Zhang A, Li R, Sun D, Li W, Zhao L et al (2019) Rab5-dependent autophagosome closure by ESCRT. *J Cell Biol* 218: 1908–1927
- Zhu L, Jorgensen JR, Li M, Chuang Y-S, Emr SD (2017) ESCRTs function directly on the lysosome membrane to downregulate ubiquitinated lysosomal membrane proteins. *eLife* 6: e26403
- Zimmer T, Vogel F, Ohta A, Takagi M, Schunck WH (1997) Protein quality—a determinant of the intracellular fate of membrane-bound cytochromes P450 in yeast. *DNA Cell Biol* 16: 501–514
- van Zutphen T, Todde V, de Boer R, Kreim M, Hofbauer HF, Wolinski H, Veenhuis M, van der Klei IJ, Kohlwein SD (2014) Lipid droplet autophagy in the yeast *Saccharomyces cerevisiae*. *Mol Biol Cell* 25: 290–301



License: This is an open access article under the terms of the Creative Commons Attribution-NonCommercial-NoDerivs 4.0 License, which permits use and distribution in any medium, provided the original work is properly cited, the use is non-commercial and no modifications or adaptations are made.